

Turbulence Model Effects on Cold-Gas Lateral Jet Interaction in a Supersonic Crossflow

by James DeSpirito

ARL-TR-6963

June 2014

NOTICES

Disclaimers

The findings in this report are not to be construed as an official Department of the Army position unless so designated by other authorized documents.

Citation of manufacturer's or trade names does not constitute an official endorsement or approval of the use thereof.

Destroy this report when it is no longer needed. Do not return it to the originator.

Army Research Laboratory

Aberdeen Proving Ground, MD 21005-5066

ARL-TR-6963**June 2014**

Turbulence Model Effects on Cold-Gas Lateral Jet Interaction in a Supersonic Crossflow

James DeSpirito

Weapons and Materials Research Directorate, ARL

REPORT DOCUMENTATION PAGE			Form Approved OMB No. 0704-0188		
<p>Public reporting burden for this collection of information is estimated to average 1 hour per response, including the time for reviewing instructions, searching existing data sources, gathering and maintaining the data needed, and completing and reviewing the collection information. Send comments regarding this burden estimate or any other aspect of this collection of information, including suggestions for reducing the burden, to Department of Defense, Washington Headquarters Services, Directorate for Information Operations and Reports (0704-0188), 1215 Jefferson Davis Highway, Suite 1204, Arlington, VA 22202-4302. Respondents should be aware that notwithstanding any other provision of law, no person shall be subject to any penalty for failing to comply with a collection of information if it does not display a currently valid OMB control number.</p> <p>PLEASE DO NOT RETURN YOUR FORM TO THE ABOVE ADDRESS.</p>					
1. REPORT DATE (DD-MM-YYYY)		2. REPORT TYPE		3. DATES COVERED (From - To)	
June 2014		Final		January 2013–January 2014	
4. TITLE AND SUBTITLE Turbulence Model Effects on Cold-Gas Lateral Jet Interaction in a Supersonic Crossflow			5a. CONTRACT NUMBER		
			5b. GRANT NUMBER		
			5c. PROGRAM ELEMENT NUMBER		
6. AUTHOR(S) James DeSpirito			5d. PROJECT NUMBER		
			AH80		
			5e. TASK NUMBER		
7. PERFORMING ORGANIZATION NAME(S) AND ADDRESS(ES) U.S. Army Research Laboratory ATTN: RDRL-WML-E Aberdeen Proving Ground, MD 21005-5066			5f. WORK UNIT NUMBER		
			8. PERFORMING ORGANIZATION REPORT NUMBER		
			ARL-TR-6963		
9. SPONSORING/MONITORING AGENCY NAME(S) AND ADDRESS(ES)			10. SPONSOR/MONITOR'S ACRONYM(S)		
			11. SPONSOR/MONITOR'S REPORT NUMBER(S)		
12. DISTRIBUTION/AVAILABILITY STATEMENT Approved for public release; distribution is unlimited.					
13. SUPPLEMENTARY NOTES					
14. ABSTRACT Computational fluid dynamic predictions of surface pressures resulting from a sonic lateral jet venting into a supersonic crossflow from a cone-cylinder-flare missile are compared to archival wind tunnel data. Predictions of axial and azimuthal pressure profiles were found to be very dependent on turbulence model, with some models performing relatively poorly. Menter's Baseline Model gave very good to excellent predictions and was used to perform additional validations of other flow conditions, jet nozzle configurations, and jet pressure ratios, again with excellent agreement. The study detailed in this report found that, even with the observed variations in surface pressure, the aerodynamic forces and moments produced by the lateral jet interaction were much less sensitive to the turbulence model. However, an estimate of the trajectory and strength of the counter-rotating vortex pair showed that while there was little effect of turbulence model on the location of the vortex pair, the induced vorticity varied by over 30%. This difference can be large enough to impact the prediction of the resultant forces and moments if there are fins or other appendages in the wake of the counter-rotating vortex pair.					
15. SUBJECT TERMS lateral jet, computational fluid dynamics, aerodynamics					
16. SECURITY CLASSIFICATION OF:			17. LIMITATION OF ABSTRACT	18. NUMBER OF PAGES	19a. NAME OF RESPONSIBLE PERSON
a. REPORT	b. ABSTRACT	c. THIS PAGE			James DeSpirito
Unclassified	Unclassified	Unclassified	UU	60	19b. TELEPHONE NUMBER (Include area code) 410-306-0778

Standard Form 298 (Rev. 8/98)
Prescribed by ANSI Std. Z39.18

Contents

List of Figures	iv
List of Tables	vi
Acknowledgments	vii
1. Introduction	1
2. Approach	3
2.1 Cone-Cylinder-Flare (CCF) Missile Models.....	3
2.2 Computational Details	4
2.2.1 Computational Domains.....	4
2.2.2 CFD Solver	8
2.2.3 Flow and Boundary Conditions.....	9
2.3 Jet Amplification Factors	10
3. Results and Discussion	11
3.1 ISL Model.....	11
3.1.1 CFD Validation Results.....	11
3.1.2 Turbulence Model Effects on ISL Model Results	13
3.1.3 Comparison With ISL CFD.....	18
3.2 DLR Model.....	19
3.2.1 Validation Results	19
3.2.2 Comparison With ISL CFD With DLR Model	29
3.2.3 Turbulence Model Effects on DLR Model Results	30
4. Summary and Conclusions	40
5. References	42
List of Symbols, Abbreviations, and Acronyms	45
Distribution List	48

List of Figures

Figure 1. Key features of a jet interaction flowfield around a body of revolution.	2
Figure 2. (a) ISL and (b) DLR wind tunnel models.....	4
Figure 3. ISL model with (a) freestream; (2) wind tunnel computational domain; and (c) side view of jet nozzle and generic plenum.	5
Figure 4. DLR model with (a) single-jet; (b) multi-jet computational domains; and (c) side view of single-jet nozzle and generic plenum chamber.....	6
Figure 5. Typical nondimensional wall distance along upper and lower missile body symmetry plane.....	7
Figure 6. Mach number contours on symmetry plane and C_p contours on ISL missile model surfaces in $M = 3.0$ crossflow, MBL turbulence model; (a) full domain, PR = 97, and near-jet region with (b) PR = 50, (c) PR = 70, and (d) PR = 97.	12
Figure 7. Surface pressure profiles (left) longitudinally along missile axis and (right) azimuthally around body for (a) PR = 50, (b) PR = 70, and (c) PR = 97 using MBL turbulence model, $M = 3.0$, $\alpha = 0^\circ$	14
Figure 8. Effect of compressibility correction using MBL turbulence model on (a) longitudinal and (b) azimuthal pressure profiles, $M = 3.0$, $\alpha = 0^\circ$, PR = 97.....	15
Figure 9. Effect of turbulence model: $k-\omega$ -based models, on (a) longitudinal and (b) azimuthal pressure profiles, $M = 3.0$, $\alpha = 0^\circ$, PR = 97.	15
Figure 10. Effect of turbulence model: MBL and $k-\varepsilon$ -based models on (a) longitudinal and (b) azimuthal pressure profiles, $M = 3.0$, $\alpha = 0^\circ$, PR = 97.	16
Figure 11. Effect of turbulence model: MBL and SA-based models on (a) longitudinal and (b) azimuthal pressure profiles, $M = 3.0$, $\alpha = 0^\circ$, PR = 97.	17
Figure 12. Mach contours on symmetry and exit planes and C_p on missile surfaces for 1- (left), 2- (middle), and 3-jet (right) configurations; (a) $\alpha = -10^\circ$, (b) $\alpha = 0^\circ$, (c) $\alpha = 10^\circ$, and (d) $\alpha = 15^\circ$, $M = 3.0$, PR = 150 ($-0.10 \leq C_p \leq 0.15$; $0 \leq M \leq 3.6$).	20
Figure 13. Comparison of predicted and experimental longitudinal C_p profiles at (a) $\alpha = 0^\circ$, (b) $\alpha = 10^\circ$, (c) $\alpha = -5^\circ$, and (d) $\alpha = -10^\circ$ for single-jet case; $M = 2.8$, PR = 100, $\phi = 180^\circ$	21
Figure 14. Comparison of predicted and experimental longitudinal C_p profiles at (a) $\alpha = 0^\circ$, (b) $\alpha = 10^\circ$, (c) $\alpha = -5^\circ$, and (d) $\alpha = -10^\circ$, $M = 2.8$ for single-jet case; PR = 100, $\phi = 150^\circ$	22
Figure 15. Comparison of predicted and experimental longitudinal C_p profiles at (a) $\alpha = 0^\circ$, (b) $\alpha = 10^\circ$, (c) $\alpha = -5^\circ$, and (d) $\alpha = -10^\circ$ for single-jet case; $M = 2.8$, PR = 100, $\phi = 120^\circ$	23
Figure 16. Comparison of predicted and experimental azimuthal C_p profiles for $\alpha = 0^\circ$ (left), $\alpha = 10^\circ$ (middle), and $\alpha = -10^\circ$ (right) at (a) $X/D = 4.0$, (b) $X/D = 4.9$, (c) $X/D = 5.9$, and (d) $X/D = 6.1$ for single-jet case; $M = 2.8$, PR = 100.....	24

Figure 17. Comparison of predicted and experimental longitudinal ΔC_p profiles at (a) $\phi = 180^\circ$, (b) $\phi = 150^\circ$, (c) $\phi = 120^\circ$, and (d) $\phi = 90^\circ$ for single-jet case; $M = 3.0$, $PR = 200$, $\alpha = 0^\circ$.	25
Figure 18. Comparison of predicted and experimental longitudinal ΔC_p profiles at (a) $PR = 55$, (b) $PR = 110$, (c) $PR = 150$, and (d) $PR = 200$ for single-jet case; $M = 3.0$, $\phi = 180^\circ$, $\alpha = 0^\circ$.	26
Figure 19. Comparison of predicted and experimental longitudinal ΔC_p profiles at (a) $\alpha = -10^\circ$, (b) $\alpha = 0^\circ$, (c) $\alpha = 10^\circ$, and (d) $\alpha = 15^\circ$ for single-jet case; $M = 3.0$, $\phi = 180^\circ$, $PR = 150$.	27
Figure 20. Comparison of predicted and experimental longitudinal ΔC_p profiles at (a) $\alpha = -10^\circ$, (b) $\alpha = 0^\circ$, (c) $\alpha = 10^\circ$, and (d) $\alpha = 15^\circ$ for 2-jet case; $M = 3.0$, $\phi = 180^\circ$, $PR = 150$.	28
Figure 21. Comparison of predicted and experimental longitudinal ΔC_p profiles at (a) $\alpha = -10^\circ$, (b) $\alpha = 0^\circ$, (c) $\alpha = 10^\circ$, and (d) $\alpha = 15^\circ$ for 3-jet case; $M = 3.0$, $\phi = 180^\circ$, $PR = 150$.	29
Figure 22. Effect of $k-\omega$ -based turbulence models on 1-jet DLR case: $M = 3.0$, $PR = 200$, $\alpha = 0^\circ$, and (a) $\phi = 180^\circ$, (b) $\phi = 150^\circ$, (c) $\phi = 120^\circ$, and (d) $\phi = 90^\circ$.	31
Figure 23. Effect of MBL and $k-\varepsilon$ -based turbulence models on 1-jet DLR case: $M = 3.0$, $PR = 200$, $\alpha = 0^\circ$, and (a) $\phi = 180^\circ$, (b) $\phi = 150^\circ$, (c) $\phi = 120^\circ$, and (d) $\phi = 90^\circ$.	32
Figure 24. Effect of MBL and SA-based turbulence models on 1-jet DLR case: $M = 3.0$, $PR = 200$, $\alpha = 0^\circ$, and (a) $\phi = 180^\circ$, (b) $\phi = 150^\circ$, (c) $\phi = 120^\circ$, and (d) $\phi = 90^\circ$.	33
Figure 25. Effect of (a) $k-\omega$ -based, (b) MBL and $k-\varepsilon$ -based, and (c) MBL and SA-based turbulence models on 1-jet DLR case $M = 3.0$, $PR = 200$, $\phi = 180^\circ$, and $\alpha = 10^\circ$.	34
Figure 26. Velocity magnitude contours on symmetry plane and vorticity contours on five axial planes along flare section.	36
Figure 27. Variation of location of maximum symmetry plane vorticity with missile axial location and turbulence model.	37
Figure 28. Variation of maximum vorticity with missile axial location and turbulence model.	38
Figure 29. Simulated surface oil flow streamlines and C_p contours ($-0.10 \leq C_p \leq 0.15$) on surface of missile for cases with (a) MBL, (b) SST, (c) kw, (d) rkw, (e) SA, (f) SARC, (g) rke, (h), cke, and (i) keR turbulence models.	39

List of Tables

Table 1. Meshes investigated for ISL NJ and single-jet configurations.	6
Table 2. Wind tunnel crossflow boundary conditions.	9
Table 3. Summary of turbulence model effects on force and moment data, $M = 3.0$, $\alpha = 0^\circ$, PR = 97.	18
Table 4. Summary of force and moment validation data, MBL turbulence model, $M = 3.0$, $\alpha = 0^\circ$, PR = 97.	19
Table 5. Summary of ARL CFD predicted force and moment data, MBL TM, $M = 2.8$	30
Table 6. Summary of ISL CFD (11) predicted force and moment data, SST TM, $M = 2.8$	30
Table 7. Summary of turbulence model effects, $M = 3.0$, PR = 200, $\alpha = 0^\circ$ ($F_j = -42.8$ N).....	35
Table 8. Summary of turbulence model effects, $M = 3.0$, PR = 200, $\alpha = 10^\circ$	35
Table 9. Variation of location of maximum symmetry plane vorticity with missile axial location and turbulence model (all distances in mm).	37
Table 10. Variation of maximum vorticity with missile axial location and turbulence model.	38

Acknowledgments

This work was performed under the auspices of The Technical Cooperation Program (TTCP) under Key Technology Area (KTa) 2–30, “Reaction Control Jets for Weapons,” led by the author, and the unlimited release of these results was agreed to by all participating member organizations. The author thanks Dr. Ross Chaplin, Defence Science Technology Laboratory, United Kingdom (UK), and Dr. David MacManus and Robert Christie, Cranfield University, UK, for supplying the digitized experimental data found in the work by P. Gnemmi and H. J. Schafer, “Experimental and Numerical Investigations of a Transverse Jet Interaction on a Missile Body, AIAA-2005-0052,” (2005). The work described in this report was supported in part by a grant of high-performance computing time from the U.S. Department of Defense (DOD) High Performance Computing Modernization program at the U.S. Army Research Laboratory DOD Supercomputing Resource Center (DSRC), Aberdeen Proving Ground, MD. The author would also like to thank Ms. Karen R. Heavey for providing a technical review of the manuscript.

INTENTIONALLY LEFT BLANK.

1. Introduction

The study of jets issuing into a crossflow has been investigated for about 70 years (1) and occur commonly in both nature (e.g., volcano and fire plumes) and engineering technology (2). It has been established that the operation of a lateral reaction jet in atmospheric flight for maneuver control of a missile or projectile results in an interference flow between the jet plume and the flow over the vehicle (3, 4). This jet interaction (JI) can have a significant effect on the resulting forces and moments imparted by the jet onto the vehicle. Accurate prediction of both the amplification and/or attenuation of these forces and moments and their effective point of action are critical to the accuracy of any flight trajectory simulations using an aerodynamic model based on these simulations (5–7). Due to its importance in this area and other areas such as fuel injection into air-breathing engine combustors (2), lateral jet injection into crossflows is still an active area of research (8).

The flow structure in the near field of a supersonic jet issuing from a body of revolution (i.e., a projectile or missile) is shown in figure 1. The flow structure is similar to that of a lateral jet issuing from a flat plate, but now the jet is located behind the bow shock formed at the nose of the missile in a supersonic crossflow. Also, the jet bow shock and the counter-rotating horseshoe vortices that emanate from the separation region will tend to wrap-around the projectile body. As with the flow structure on a flat plate, a shock-boundary layer interaction forms upstream of the jet leading to a flow separation region and a λ -shock structure. A barrel shock surrounds the jet plume and terminates in a Mach disk. The most dominant feature is usually a counter-rotating vortex pair (CVP) formed by the jet wake that travels downstream. The low-pressure region behind the jet is usually the major contributor to the attenuation of the jet thrust force observed on bodies of revolution. The CVP and horseshoe vortices may also interact with the missile surface or appendages and further modify the resultant forces and moments on the missile.

The availability of new validation data on bodies of revolution, especially providing both surface pressure and force and moment data, is somewhat limited. Wind tunnel data gathering surface pressure, oil flow, and perhaps particle image velocimetry (PIV) data is very useful, but usually does not also include the forces and moments on the model. Also, for practical reasons at the wind tunnel test facility, the data is usually taken with a single-species, cold-jet gas (i.e., facility room temperature), rather than a multispecies gas at the flame temperature of the combustion products of the gas generator. If flight test data is available, then only force and moment data may be extracted, which can also be difficult to accurately determine from the flight data available.

One series of experimental data appropriate for validation of computational fluid dynamics (CFD) simulations was recently published by researchers from the French-German Research Institute of Saint-Louis (ISL) in Saint-Louis, France (9–11) and the German Aerospace Center

(DLR) in Braunschweig, Germany (10–13). These studies involved wind tunnel investigations of radial cold-gas ejection from one to three sonic nozzles on a cone-cylinder-flare (CCF) missile in supersonic crossflows of Mach 2.8 and 3.0. Jet pressure ratios (PR) of 50 to 300 were investigated and data included wall surface pressures measured from pressure taps arranged in four longitudinal sections and up to four azimuthal sections in addition to some oil flow visualizations. Some data for the DLR model was obtained for a hot-gas jet (11) for which the model diameter was 70 mm, but the jet nozzle diameter remained 4 mm. More recent results from these authors include additional results from wind tunnel investigations on hot-gas lateral jet ejection (14, 15) and substitution of hot-gas lateral jets by cold-gas simulants in supersonic flow (16).

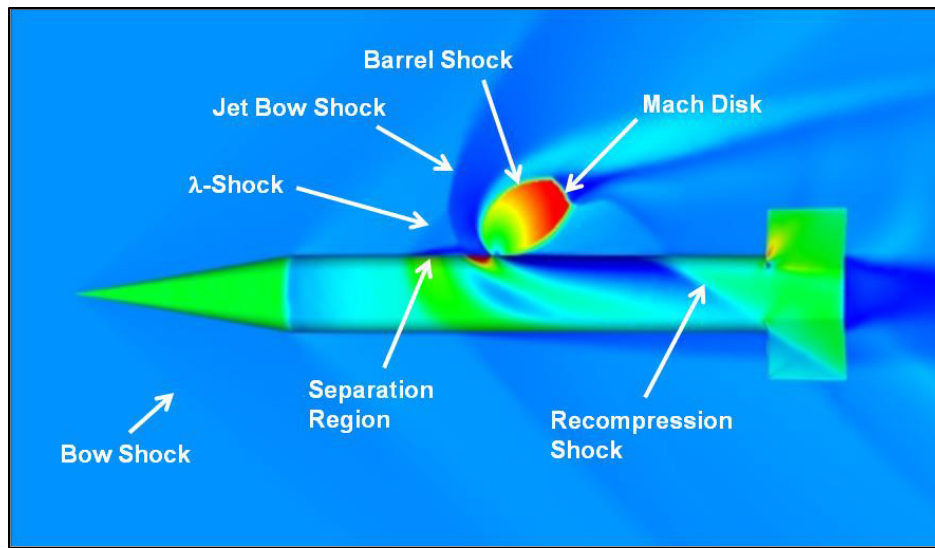


Figure 1. Key features of a jet interaction flowfield around a body of revolution (5, 7).

The objective of the present study is to use the published experimental data from the ISL and DLR wind tunnel investigations to quantify the accuracy of CFD in predicting the pressure profiles on the CCF missile surface due to the jet interaction with the supersonic crossflow. Specifically, the effect of the turbulence model employed on the resulting pressure distribution and JI force and moment are determined. Previous results have shown that the pressure profiles induced by the jet interaction can be highly dependent on the turbulence model employed in the calculation (5–7). It was also observed in those studies that the resulting JI force variation with turbulence model was less than 10%, even though the prediction of the flow separation and reattachment varied significantly. The JI moment, however, did have a larger variation with turbulence model. This is an important observation, since it means that the computational aerodynamicist may be able to provide JI aerodynamic force and moment data for flight simulations with less variation with turbulence model than indicated by the surface pressure profiles.

This work was performed as part of a research activity under the auspices of The Technical Cooperation Program (TTCP), an “international organization that collaborates in defense scientific and technical information exchange; program harmonization and alignment; and shared research activities for the five nations (17).” The five nations were Australia, Canada, New Zealand, the United Kingdom (UK), and the United States.

2. Approach

2.1 Cone-Cylinder-Flare (CCF) Missile Models

The ISL (9) and DLR (10–13) CCF missile models are shown in figures 2a and 2b, respectively. They consisted of a $2.8 D$ long conical nose ($D = 40$ mm), a $3.2 D$ long cylindrical section, and a $3 D$ long flared afterbody with a $1.66 D$ base diameter. * The jet nozzle in the ISL model was a circular, sonic nozzle of diameter $0.1 D$ ($d = 4$ mm) located on the cylindrical section at a position $4.2 D$ from the nose ($1.4 D$ from the cone-cylinder shoulder). The DLR model contained either one (10, 11, 13) or three (12) side jet sonic nozzles of $0.1 D$ located $4.3 D$ from the missile nose at azimuthal angles of $\phi = 180^\circ$ (jet 1), $\phi = 150^\circ$ (jet 2), and $\phi = 120^\circ$ (jet 3) (see figure 2b). The azimuthal angles were measured clockwise around the missile when viewed from the rear with the 0° position at the bottom.

The ISL model (9) contained two series of surface pressure taps, 22 in a longitudinal section and 8 in an azimuthal section, with both sections containing the jet nozzle (figure 2a). The longitudinal section spanned approximately from $0.45 D$ in front of the jet nozzle to $0.25 D$ behind the nozzle. The azimuthal section spanned from approximately $188 \leq \phi \leq 220^\circ$. The DLR model (10–13) contained 148 static pressure taps arranged in four longitudinal rows (figure 2b). In some cases (11, 13), an additional series of four azimuthal rows of pressure taps were located at axial locations of $4.0 D$, $4.9 D$, $5.9 D$, and $6.1 D$ from the missile nose, as shown in figure 2b.

The data from the ISL model in figure 2a provides a higher level of resolution of the pressure profiles in the near-region of the jet, while the additional range of pressure taps in the DLR model shown in figure 2b provides jet interaction data much further downstream. Note that the DLR model was also tested in the ISL wind tunnel (10, 11).

The experimental data from figures in the ISL (9) and DLR publications (10–13) was digitized by the author for direct comparisons with CFD predictions. Digitized experimental data (9–12) and CFD predicted data (9) were also provided by Professor David MacManus, Cranfield University, through Dr. Ross Chaplin, Defence Science Technology Laboratory, UK.

*For explanations of symbols and abbreviations used in the text of the report, tables, figures, and equations refer to the List of Symbols, Abbreviations, and Acronyms.

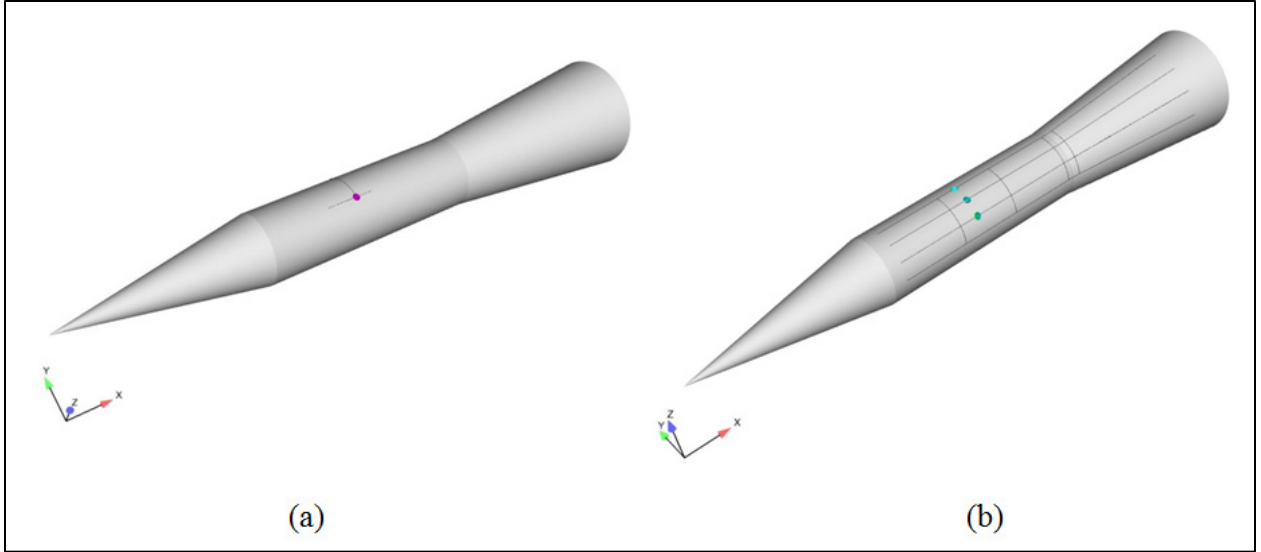


Figure 2. (a) ISL and (b) DLR wind tunnel models.

2.2 Computational Details

2.2.1 Computational Domains

The computational domains used for the ISL model were the same as reported by Gnemmi and Schafer (9), where both a freestream and wind tunnel computational domain were compared (figure 3a, b). Only one-half of the domain was modeled, taking advantage of the symmetry of the geometry. The computational domains were meshed with MIME from Metacomp Technologies (18). In both computational domains, the forward surface of the domain was a conical section located $0.5 D$ in front of the missile nose and the downstream section ended at the end of the flare section of the missile. In the freestream version the outer radial surface was located $5 D$ from the missile axis while in the wind tunnel version it was located at $2.5 D$ with boundary layer spacing adjacent to the wind tunnel wall surface. Mesh density boxes were used to refine the mesh in the region of the jet nozzle and further downstream. A generic plenum (figure 3c) was added to the cylindrical jet nozzle, but some comparisons using just the cylindrical nozzle without a plenum chamber showed very little effect on the pressure profiles outside the nozzle.

The computational domains for the DLR models were the same dimensions as the freestream version of the ISL model previously described (figure 4a, b). One-half the domain was again used for the single-jet case but the 2- and 3-jet cases required full three-dimensional (3-D) domains since the nozzles were not symmetric (figure 4b). A generic plenum was again added to the cylindrical jet nozzles but was now shaped as a hemisphere to accommodate up to three nozzles (figure 4c).

A summary of the mesh sizes investigated is shown in table 1. A mesh sensitivity study was performed with a no-jet (NJ) case to determine the overall mesh size parameters. Mesh 2 was deemed adequate from the NJ simulations using the freestream mesh version and this mesh was used as the basis for the jet-case configurations. Mesh refining in the cases with a jet nozzle consisted of placement and adjustment of density boxes in the regions affected by the jet plume. Mesh 2A (9.9 million [M] cells) was deemed adequate for the freestream version and Mesh 2B (10.9 M cells) was deemed adequate for the wind tunnel version of the final meshes. The wind tunnel version of the mesh was chosen for the analysis of the ISL model for the most direct comparison to the results from Gnemmi and Schafer (9). Higher density meshes 2C and 2D showed very little effect on the resulting surface pressure profiles. A full-domain version (2B-1, 21.8 M cells) was also investigated to determine if there was any effect of using the symmetry boundary and no effect was observed.

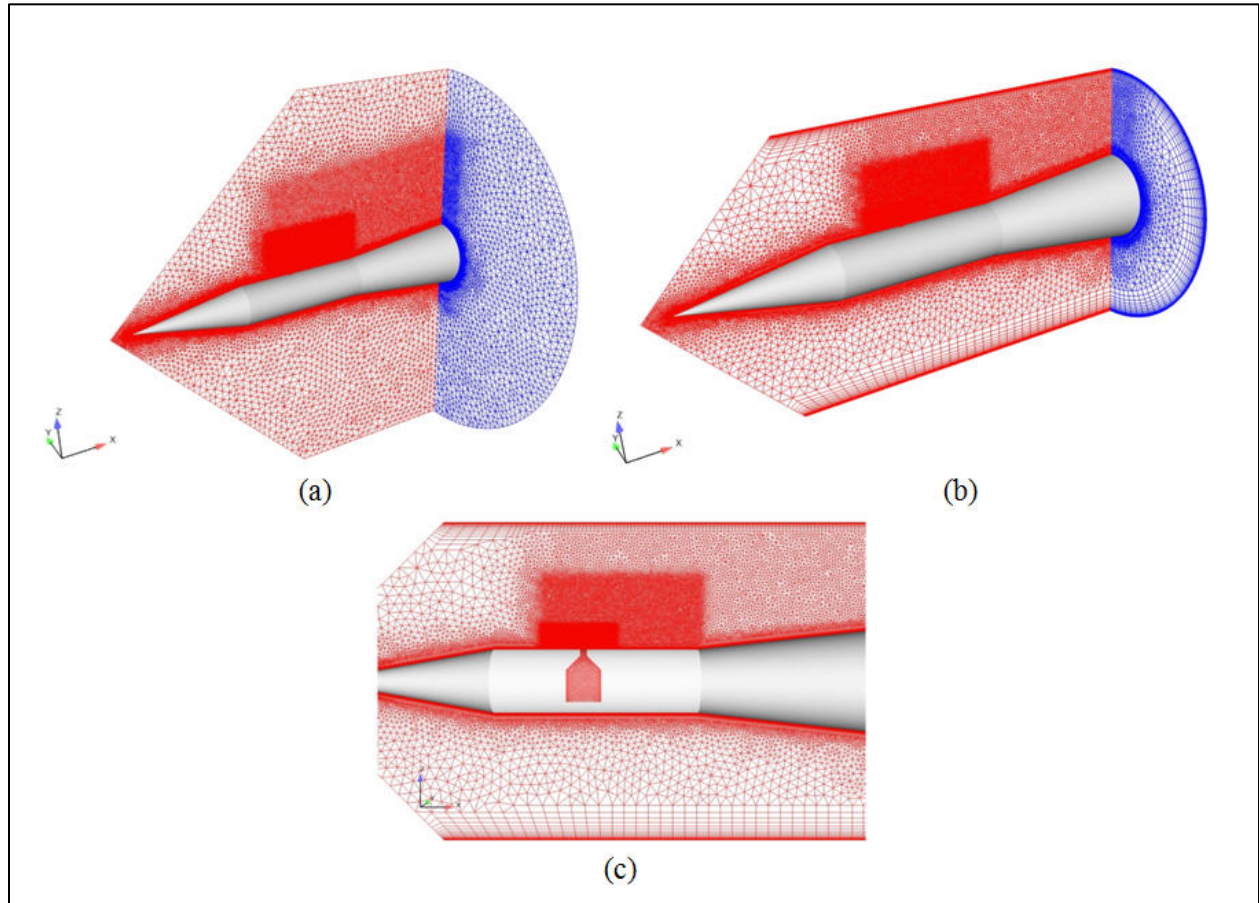


Figure 3. ISL model with (a) freestream; (b) wind tunnel computational domain; and (c) side view of jet nozzle and generic plenum.

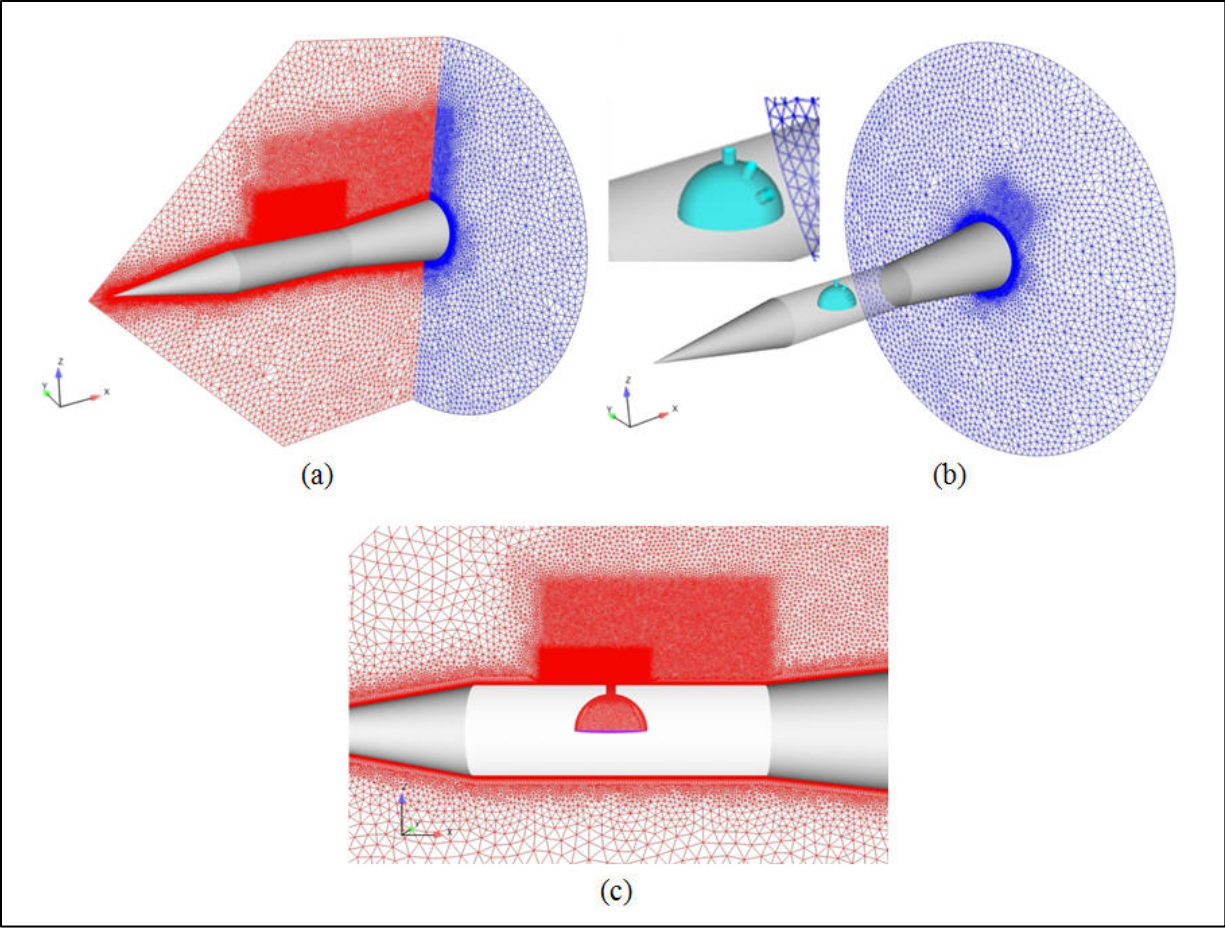


Figure 4. DLR model with (a) single-jet; (b) multi-jet computational domains; and (c) side view of single-jet nozzle and generic plenum chamber.

Table 1. Meshes investigated for ISL NJ and single-jet configurations.

Freestream Version		Wind Tunnel Version	
Mesh	No. Cells ($\times 10^6$)	Mesh	No. Cells ($\times 10^6$)
Mesh 1 (NJ)	2.7	Mesh 2	4.3
Mesh 2 (NJ)	4.4	Mesh 2A	9.6
Mesh 3 (NJ)	6.8	Mesh 2B	10.9
—	—	Mesh 2B-1 (Full)	21.8
Mesh 2	6.2	Mesh 2C	16.4
Mesh 2A	9.9	Mesh 2D	24.9

The mesh characteristics for the DLR model with single and multiple jets were based on the ISL model Mesh 2B, but expanded radially into a freestream mesh (figure 4). The one-half physical domain mesh for the 1-jet case was 11.2 M cells, while the 2- and 3-jet configurations with a full physical domain were 21.7 M and 24.2 M cells, respectively.

Prism layers were used along all solid boundaries, including the nozzle plenum wall and throat, with the first cell wall spacing set to 1×10^{-6} m. The missile surfaces were modeled using the “solve-to-wall” methodology with y^+ values less than 0.5, except near the jet orifice, where y^+ values approach 1.0. The y^+ values can be much larger on the nozzle exit wall due to the much different flow properties there from the gas expansion. Therefore, the nozzle plenum and throat were modeled with an advanced, two-layer wall function boundary condition that reverts to a solve-to-wall method where the mesh is fine enough or else to a wall function, as appropriate. Figure 5 shows typical y^+ profiles on the upper ($\phi = 180^\circ$) and lower ($\phi = 0^\circ$) surfaces of the ISL missile at $\alpha = 0^\circ$ and PR = 97. The values are symmetric along the cone and body prior to the jet (about $X/D = -0.49$). The lower surface y^+ values remain below about 0.4, while the upper surface y^+ values are affected by the jet interaction flow properties and reach about 0.8 just ahead of the jet nozzle ($X/D = -0.1$). The peak ($y^+ = 2.1$) at $X/D = -4.18$ is due to the stagnation at the nose of the projectile, while the peaks ($y^+ = 3.7$) at $X/D = \pm 0.05$ are due to the flow properties inside the jet nozzle expanding over the edge of the exit orifice.

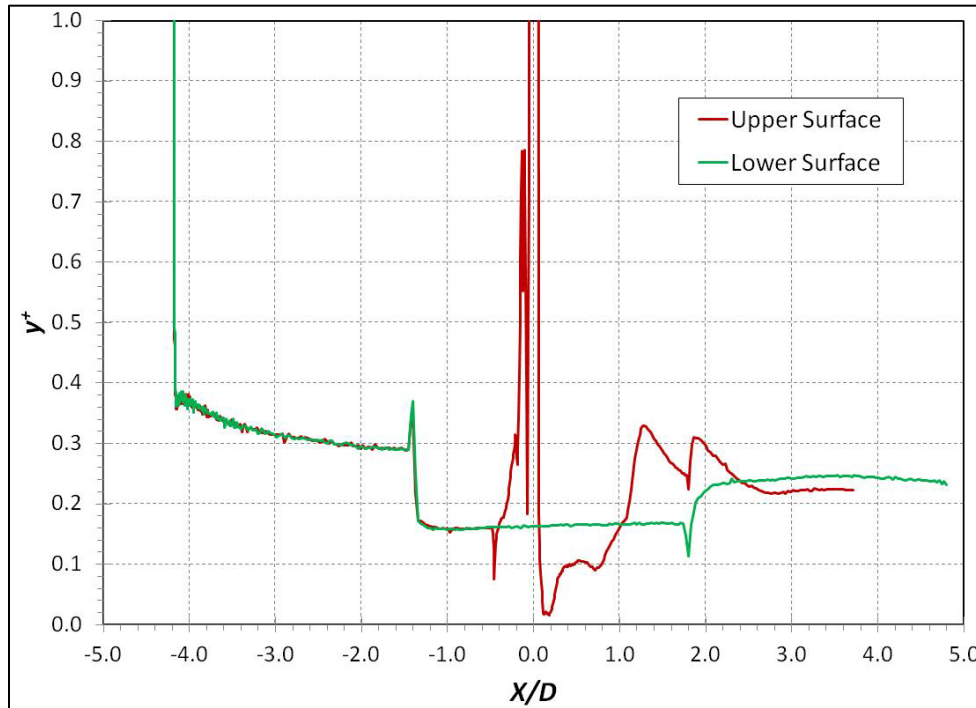


Figure 5. Typical nondimensional wall distance along upper and lower missile body symmetry plane.

2.2.2 CFD Solver

The commercially available CFD⁺⁺ code (19) version 12.1 was used in this study. The 3-D, compressible, Reynolds-Averaged Navier-Stokes (RANS) equations are solved using a finite volume method. A point-implicit time integration scheme with local time-stepping, defined by the Courant-Friedrichs-Lewy (CFL) number, was used to advance the solution towards steady-state. The multigrid W-cycle method with a maximum of 4 cycles and a maximum of 20 grid levels was used to accelerate convergence. Implicit temporal smoothing was applied for increased stability, which is especially useful where strong transients arise. The inviscid flux function was a second-order, upwind scheme using a Harten-Lax-van Leer-Contact (HLLC) Riemann solver and a multidimensional Total-Variation-Diminishing (TVD) continuous flux limiter (19).

The choice of turbulence model is a key factor in the numerical modeling of complex flows such as this. CFD⁺⁺ has a large set of turbulence models available, nine of which were investigated for their accuracy in prediction of the surface pressure profiles. The nine models investigated in this study were:

1. Menter's $k-\omega$ Shear Stress Transport (SST) 2-equation model (20).
2. Menter's baseline (MBL) 2-equation model (20).
3. The standard (21) ($k\omega$).
4. Realizable (19) $k-\omega$ (rkw) 2-equation models.
5. The Spalart-Allmaras (SA) 1-equation model (22).
6. The Spalart-Allmaras 1-equation model with rotation/curvature correction (SARC) (23).
7. The realizable $k-\varepsilon$ (rke) 2-equation model (24).
8. The cubic $k-\varepsilon$ (cke) nonlinear, 2-equation model (25).
9. Goldberg's $k-\varepsilon-R_t$ (keR) 3-equation model (26).

In addition, the effect of the compressibility correction term was investigated by comparing solutions modeled with the wall-bounded and free-shear type flow options, and without the correction term.

Convergence was determined by a typical 5–6 order decrease in the magnitude of the maximum residuals and ensuring that the integrated forces and moments on the missile were not changing with increased iterations. The mass and energy flux through the jet orifice was also tracked and usually converged before the forces and moments. Typically, 5000–6000 steps were required to converge the residuals and calculations took an average of about 5–6 s of CPU time per iteration

when the mesh was partitioned with approximately 175,000 cells per CPU core. Most simulations were performed on an IBM iDataPlex Supercomputer (PERSHING) with some on a SGI Altix ICE 8200 (HAROLD), both at the U.S. Army Research Laboratory (ARL) Department of Defense (DOD) Supercomputing Resource Center (DSRC) at Aberdeen Proving Ground, MD (27).

2.2.3 Flow and Boundary Conditions

The pressure, temperature, and turbulence flow conditions for the study were obtained from the original references for the numerical and experimental studies at ISL and DLR (9–12). These conditions are summarized in table 2. The references indicate that both the ISL model and the DLR model were tested in the ISL wind tunnel. The tests in the ISL wind tunnel were only performed at $\alpha = 0$, while those performed in the DLR facility were at a range $-10^\circ \leq \alpha \leq 15^\circ$.

Jet pressure ratios of 50, 70, and 97 were investigated in the ISL facility, while jet pressure ratios of 55, 110, 150, and 300 were investigated in the DLR facility. Pressure traces were only provided in reference 12 for pressure ratios up to 200, while oil-flow visualization was provided for PR = 300. Most tests were performed at a nominal Reynolds number of 1.9×10^6 , with a lower Reynolds number of 0.5×10^6 also investigated at DLR. The total temperature of the tunnel facility for low Reynolds number tests was not explicitly stated, so the maximum total temperature of the facility was used to calculate the remaining conditions for this study. This report compares data for PR up to 200 and Reynolds numbers of 1.9×10^6 .

Table 2. Wind tunnel crossflow boundary conditions.

Test Facility	Model	M	Re	T_∞	T_0	P_∞	P_0	ρ_∞	I_t	l_t
—	—	—	$[\times 10^{-6}]$	[K]	[K]	[kPa]	[kPa]	$[\text{kg/m}^3]$	[%]	[mm]
ISL	ISL DLR	3.0	1.9	103.2	289.	19.49	715.9	0.658	0.5	2
DLR	DLR	2.8	1.9	109.0	280.	20.79	564.3	0.665	0.5	2
DLR	DLR	2.8	0.5	214.2	550.	13.17	357.5	0.214	0.5	2
DLR	DLR	3.0	1.9	100.0	280.	15.7	576.9	0.548	0.5	2

All solid surfaces were modeled as no-slip, adiabatic walls with solve-to-wall methodology on the missile body surfaces and wall functions on the nozzle plenum and throat regions for the reasons previously described. A symmetry boundary condition was used on the symmetry plane of the domain for most cases. The front and outer boundaries were modeled using a characteristics-based inflow/outflow boundary condition, which is based on solving a Riemann

problem at the boundary. For the cases modeling the wind tunnel wall, the cylindrical section of the outer boundary was modeled as a no-slip, adiabatic wall with wall functions. The exit plane was modeled with a supersonic outflow boundary condition. The inlet to the nozzle plenum was modeled as a subsonic reservoir boundary inflow with a specified total temperature and pressure. This procedure allows the nozzle exit conditions to be directly calculated during the solution.

The jet thrust is calculated by taking the difference between the computed forces on the total pressure boundary at the bottom of the plenum and the remaining plenum and the jet nozzle walls. These forces are calculated using the same tool available within CFD⁺⁺ used to calculate the forces and moments on the other surfaces. Another method within CFD⁺⁺ is to define a plane at the exit of the nozzle and use that same tool to calculate the forces and fluxes on that plane. The latter method works well when the jet nozzle axis is aligned with one of the coordinate axes. These methods can be more accurate than using the standard thrust equation, which requires some average value of the static and dynamic pressures at the jet exit.

2.3 Jet Amplification Factors

The jet amplification factor is a measure of the effect that the JI has on the control forces and moments, or the “efficiency” of the jet. The jet force and moment amplification factors are defined as

$$K_f = \frac{F_j + F_{ji}}{F_j} \quad (1)$$

and

$$K_m = \frac{M_j + M_{ji}}{M_j} . \quad (2)$$

An amplification factor greater than one indicates the JI effect increases the effectiveness of the jet thrust force, F_j , or the moment induced by the jet thrust, $M_j = F_j l_j$. If the body, such as a projectile or missile, is at an angle of attack, the force or moment induced by the angle of attack—with the jet off—is subtracted from that resulting with the jet on, e.g.,

$$F_{ji} = F_{\text{total}} - F_{\text{no-jet}} - F_j , \quad (3)$$

where F_{total} is total force due to the jet thrust, JI effects, and angle of attack. $F_{\text{no-jet}}$ is the aerodynamic force in the absence of the jet, which will be non-zero when $\alpha \neq 0$. Moments due to these forces follow directly and the equations using coefficients are similar. On a flat plate or a projectile at zero angle of attack, the JI force and moment are computed directly, since there is no force normal to the surface with the jet off. Following Gnemmi and Schafer (9), if the jet nozzle axis is located near the center of gravity, the moment amplification factor is redefined as

$$K_m = 1 + \frac{M_{ji}}{F_j D} , \quad (4)$$

since the jet moment, $M_j = F_j l_j$, goes to zero as the jet axis location approaches the center of gravity location.

3. Results and Discussion

A turbulence model study, investigating the performance of nine models, was first performed using the ISL model and the case of Mach 3.0 crossflow, $\alpha = 0^\circ$, and PR = 97. The MBL model was determined to perform the best and was used to continue the validation study using the ISL model. The ISL validation results are shown first in section 3.1.1, followed by the results of the turbulence model study in section 3.1.2. A comparison of the present CFD predictions with the ISL CFD predictions (9) is also presented via pressure traces in section 3.1.2 and force and moment data in section 3.1.3. The validation study for the DLR model using the MBL turbulence model is then presented in section 3.2.1. A comparison of the present CFD with the ISL CFD predictions (11) using the DLR model are presented in section 3.2.2. The turbulence model study was repeated using DLR model at a higher jet pressure ratio and a non-zero α in a Mach 3.0 crossflow (PR = 200, $\alpha = 0^\circ$, and $\alpha = 10^\circ$) and is presented in section 3.2.3.

3.1 ISL Model

3.1.1 CFD Validation Results

Figure 6 shows the typical jet interaction flowfield resulting from a sonic jet issuing into a supersonic crossflow. Figure 6a shows the far-field interaction for PR = 97, while figures 6b–d show the near-field interaction for PR = 50, 70, and 97, respectively. The size of the barrel shock, λ -shock, and separation and reattachment zones increases with increasing jet pressure ratio. Figure 6a shows the growth of the wind tunnel wall boundary layer and the reflection of the jet bow shock on the wind tunnel wall. The reflected shock does not impact the model.

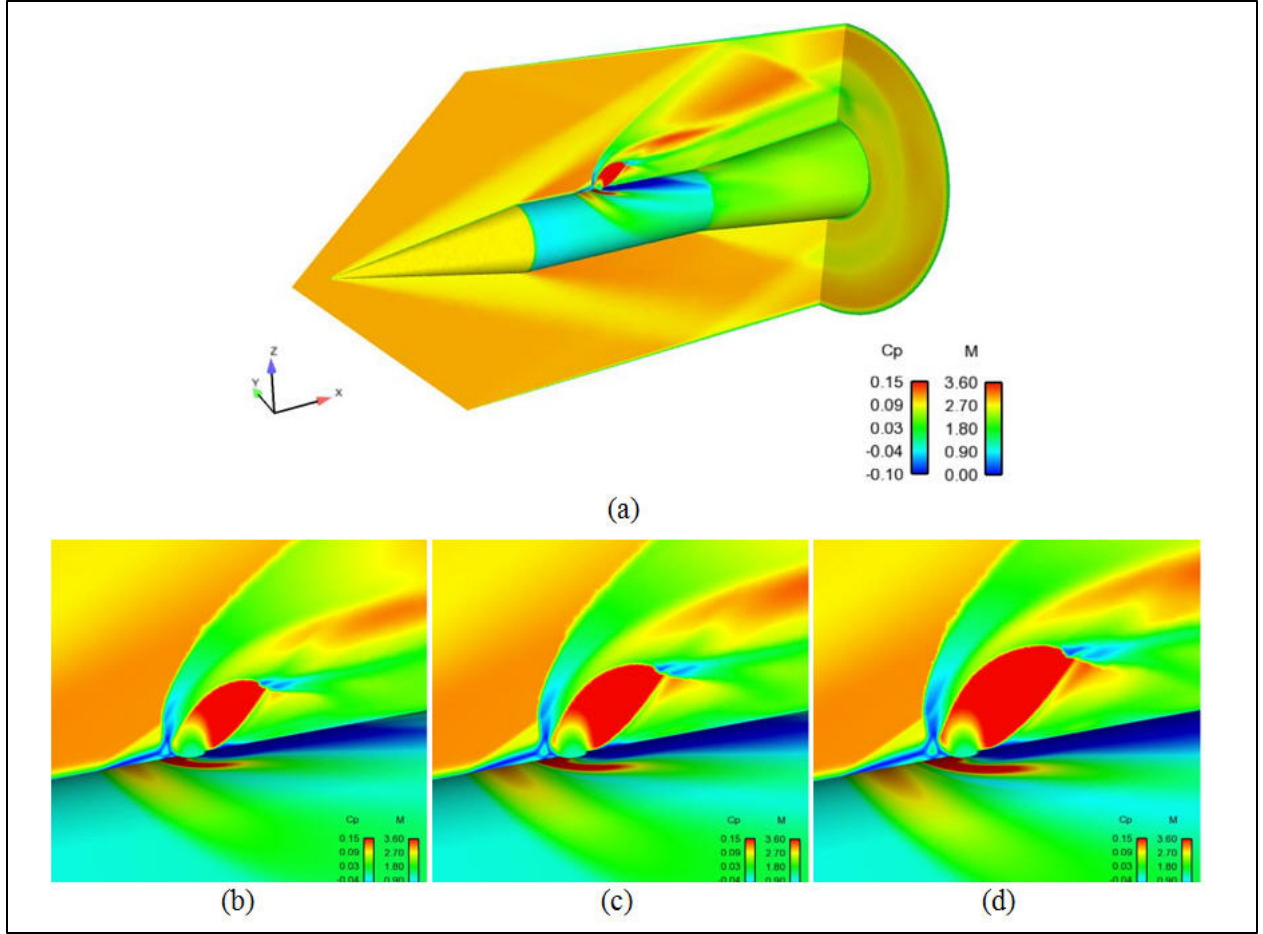


Figure 6. Mach number contours on symmetry plane and C_p contours on ISL missile model surfaces in $M = 3.0$ crossflow, MBL turbulence model; (a) full domain, $PR = 97$, and near-jet region with (b) $PR = 50$, (c) $PR = 70$, and (d) $PR = 97$.

Figure 7 shows the experimental (9) and predicted longitudinal and azimuthal C_p profiles intersecting the jet nozzle orifice for the three jet pressure ratios. The experimental data includes that digitized at both the ARL and Cranfield University. The x -scale is shifted in figures 7–11 so that the jet nozzle is located at $X/D = 0$. The features of the longitudinal profiles are typical: (1) a rise in pressure ahead of the jet nozzle where the λ -shock forms with a boundary layer separation; (2) a second, higher pressure rise indicating the main jet bow shock; (3) the nozzle exit pressure is off-scale; (4) ending with a low-pressure region behind the jet that asymptotes toward the NJ case pressure far downstream of the nozzle. The azimuthal profiles show an initial pressure rise due to the high pressure from the jet bow shock wrapping around the body followed by a lower, wider pressure rise due to the high pressure from the separation region (see figure 6).

In addition to the ARL CFD predictions using CFD^{++} , predictions from ISL (9) (digitized by Cranfield University) using the commercial code CFX-TASC flow with the SST turbulence model are shown in figures 7–11. Both predictions compare very well to the experimental data. The ARL CFD tends to predict the longitudinal and initial azimuthal pressure rise a little better

than the ISL CFD. The ISL CFD appears to predict the peak of the second azimuthal pressure rise a little better at the lower jet pressure ratios, but the ARL CFD captures the azimuthal pressure profile at $PR = 97$ better. This level of accuracy for both CFD predictions is considered very good.

3.1.2 Turbulence Model Effects on ISL Model Results

To evaluate the effect of turbulence model on the prediction of the jet interaction flowfield, nine of the turbulence models available in CFD⁺⁺ were used. The default parameters for each turbulence model were not varied. However, the effect of the compressibility correction was evaluated. Metacomp provides their version of the compressibility correction, which is used for highly compressible flows (e.g., supersonic and hypersonic flows) to alleviate the diminished diffusive mixing in the turbulent regions due to the high inertia of the flow. Once turned on, the user needs to choose the type of flow (i.e., either a “free-shear” flow or a “wall-bounded” flow). If the flow in question has both types of flow, Metacomp recommends using the “free-shear” option.

The effect of the compressibility correction on the CFD predictions using the MBL turbulence model is shown in figure 8. The results clearly show that the “free-shear” option provides the most accurate prediction of the pressure profiles. The effect of the compressibility correction using several other turbulence models was investigated and the “free-shear” option consistently gave the best results. This confirms Metacomp’s recommendation, as this flow does have both wall-bounded and free-shear zones of interest. The following results showing the effects of different turbulence models will all use the “free-shear” compressibility correction option.

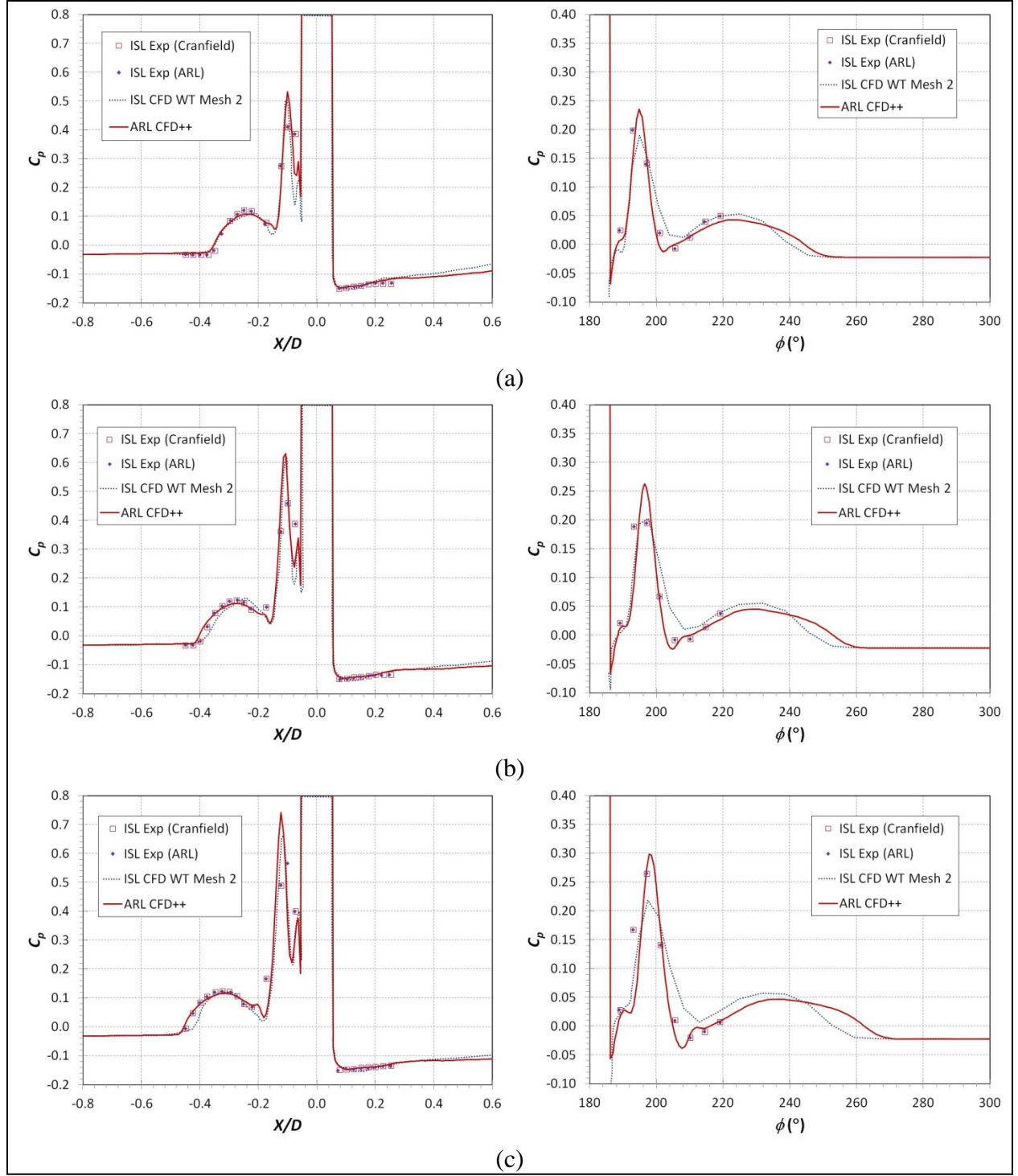


Figure 7. Surface pressure profiles (left) longitudinally along missile axis and (right) azimuthally around body for (a) PR = 50, (b) PR = 70, and (c) PR = 97 using MBL turbulence model, $M = 3.0$, $\alpha = 0^\circ$.

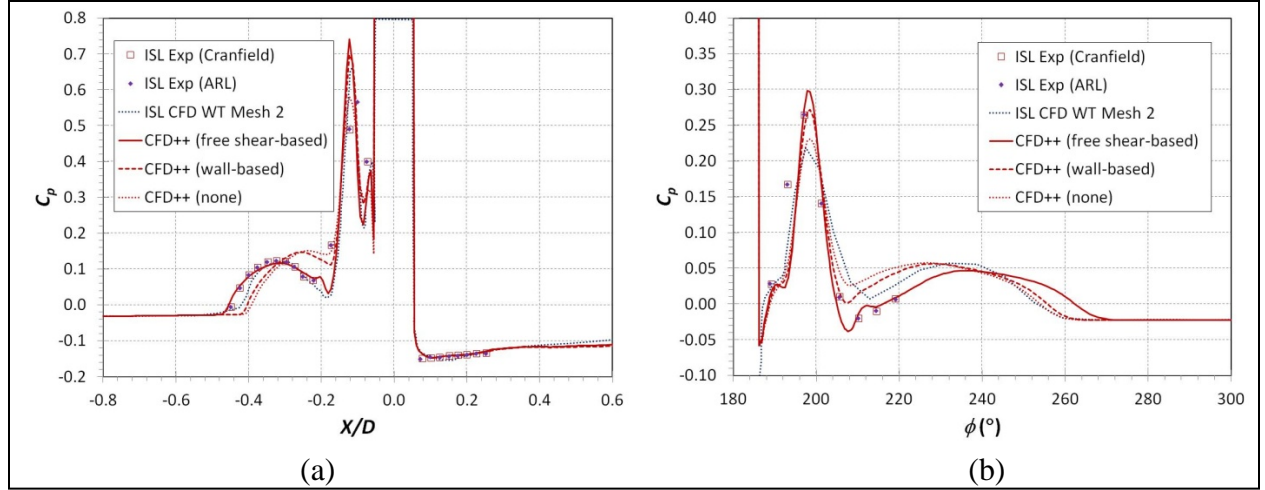


Figure 8. Effect of compressibility correction using MBL turbulence model on (a) longitudinal and (b) azimuthal pressure profiles, $M = 3.0$, $\alpha = 0^{\circ}$, PR = 97.

Figure 9 shows the variation in prediction accuracy for the $k-\omega$ -based models (MBL, SST, kw, rkw). In both the longitudinal and azimuthal directions, the MBL provides the most accurate prediction while the SST (surprisingly) provides the least accurate—overestimating the length of the forward separation region. The kw and rkw models underpredict the size of the forward separation region, but generally predict the pressure magnitude. The kw and rkw models also predict some oscillations in the pressure ahead of the bow shock. The rkw model provides the best prediction of the data after the MBL model.

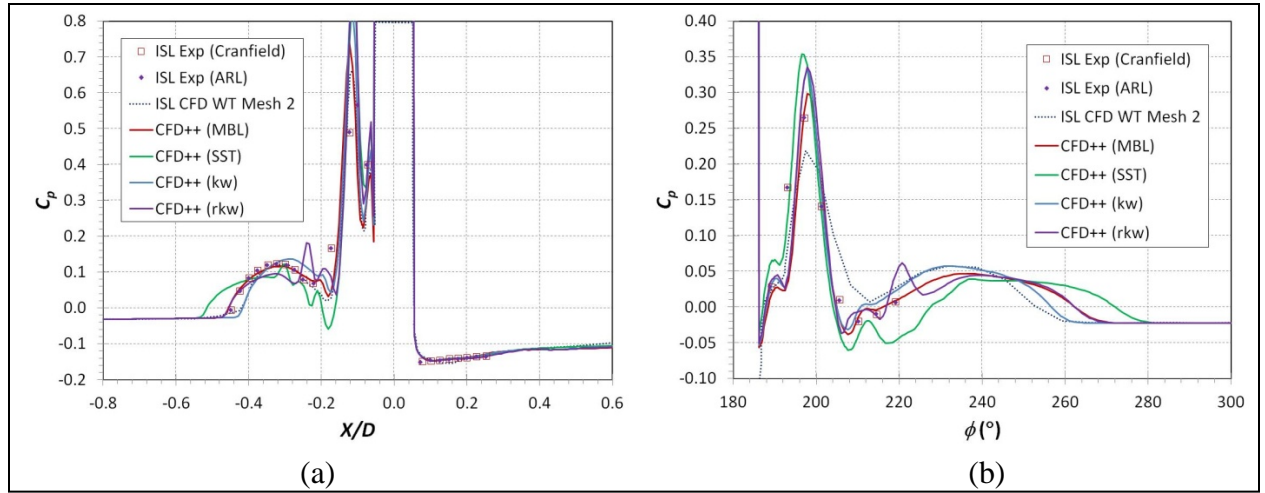


Figure 9. Effect of turbulence model: $k-\omega$ -based models, on (a) longitudinal and (b) azimuthal pressure profiles, $M = 3.0$, $\alpha = 0^{\circ}$, PR = 97.

Figure 10 shows the comparison of the prediction using the MBL model with those using the k - ε -based models (rke, cke, keR). The MBL model again provides the most accurate prediction of the pressure profiles. The rke model provides the least accurate, overpredicting the length of the forward separation region, which leads to the poor azimuthal profile prediction (figure 10b). The predictions with the cke model are also very good; however, there are some oscillations in the pressure ahead of the jet bow shock. These oscillations do not appear to be present in the experimental data, but a higher density in the number of pressure taps might be needed to determine this definitively.

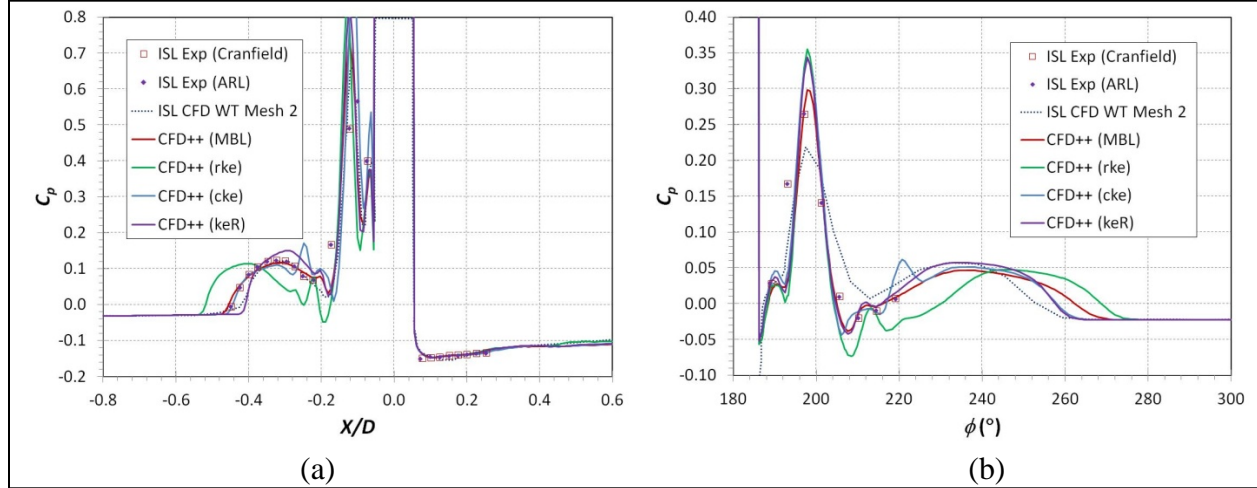


Figure 10. Effect of turbulence model: MBL and k - ε -based models on (a) longitudinal and (b) azimuthal pressure profiles, $M = 3.0$, $\alpha = 0^\circ$, PR = 97.

Figure 11 shows the comparison of the prediction using the MBL model with the SA and SARC models. The SA model performs reasonably well, but the SARC model underpredicts the size of the forward separation region and the peak pressure due to the bow shock, which leads to the poor azimuthal profile prediction (figure 11b). In general the MBL, SA, rkw, and cke models perform reasonably well at predicting the pressure profiles, with the MBL performing best overall in this test case.

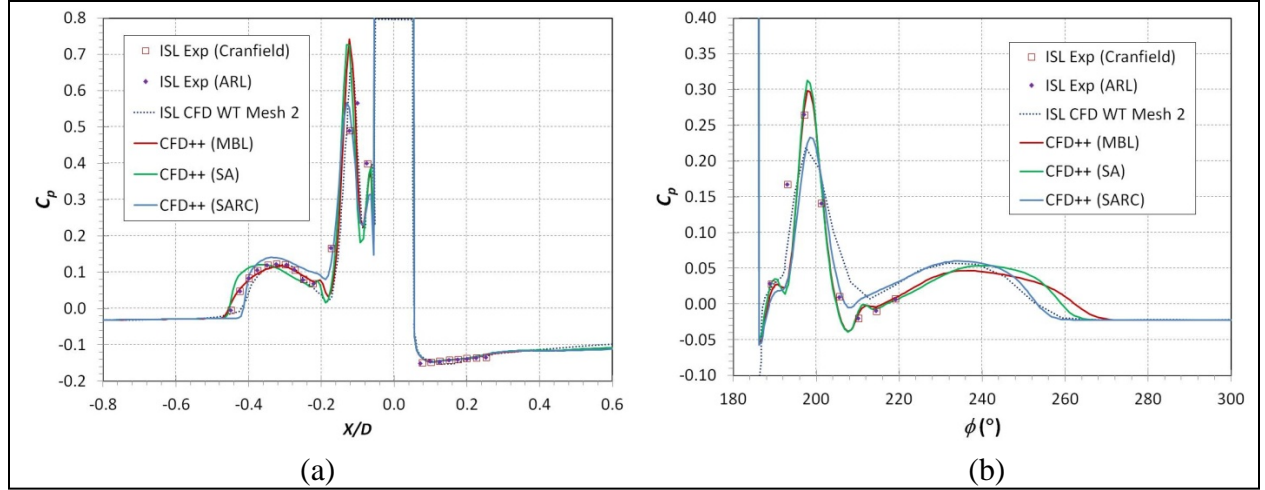


Figure 11. Effect of turbulence model: MBL and SA-based models on (a) longitudinal and (b) azimuthal pressure profiles, $M = 3.0$, $\alpha = 0^\circ$, $PR = 97$.

The accurate prediction of the surface pressures is of course very important, but the sensitivity of the variations due to turbulence model on the actual predicted forces and moments is also very important. The latter data is what is used in flight trajectory simulations to evaluate the performance of the flight vehicle. As shown in table 3, the variation in the predicted forces and moments is about 4% or less, within the expected accuracy of most CFD predictions.

These results show that the predicted force and moment data is fairly insensitive to jet nozzle near-field pressure profiles, which is dependent on the turbulence model employed. This particular missile has no appendages, such as fins, to the rear of the jet, so no jet-fin interactions can be quantified here. A previous study by the author (6, 7) showed that, on a finned missile, the effects of turbulence model was less than 6% on the JI forces, but up to 36% on the JI moment. Therefore, the appropriate selection of turbulence model is still very important to the accurate prediction of JI flowfield.

Table 3. Summary of turbulence model effects on force and moment data, $M = 3.0$, $\alpha = 0^\circ$, $PR = 97$.

TM	C_{A0}	C_N	$C_{m(0)}$	F_j	F_{ji}	$M_{ji(0)}$	M_{ji}	X_{cp}	X_{cp}/D	K_f	K_m
—	—	—	—	[N]	[N]	[N-m]	[N-m]	[m]	—	—	—
MBL	0.2513	0.1029	-0.7976	-28.2	15.9	-4.9226	-2.2549	0.3100	7.75	0.44	3.00
SST	0.2509	0.1006	-0.7752	-28.2	15.5	-4.7845	-2.1777	0.3083	7.71	0.45	2.93
kw	0.2626	0.1008	-0.7945	-28.3	15.5	-4.9033	-2.2913	0.3154	7.88	0.45	3.03
rkw	0.2523	0.0957	-0.7483	-28.3	14.8	-4.6186	-2.1370	0.3127	7.82	0.48	2.89
SA	0.2672	0.1016	-0.7931	-28.3	15.7	-4.8945	-2.2603	0.3122	7.80	0.44	3.00
SARC	0.2694	0.1050	-0.8307	-28.2	16.2	-5.1270	-2.4065	0.3166	7.92	0.43	3.13
rke	0.2535	0.0994	-0.7566	-28.2	15.3	-4.6693	-2.0929	0.3045	7.61	0.46	2.85
cke	0.2501	0.0963	-0.7633	-28.3	14.9	-4.7109	-2.2142	0.3170	7.92	0.47	2.96
keR	0.2649	0.0995	-0.7801	-28.2	15.4	-4.8145	-2.2347	0.3135	7.84	0.46	2.98
—	—	—	—	—	—	—	—	—	—	—	—
Mean	0.2580	0.1002	-0.7822	-28.2	15.5	-4.8272	-2.2299	0.3122	7.81	0.45	2.97
STD	0.0079	0.0029	0.0252	0.02	0.45	0.1554	0.0914	0.0041	0.10	0.02	0.08
%STD	3.05%	2.92%	-3.22%	-0.07%	2.92%	-3.22%	-4.10%	1.31%	1.31%	3.58%	2.73%

3.1.3 Comparison With ISL CFD

Unfortunately, the experimental validation data lacks force and moment data that would have been important to totally quantify the present CFD predictions. An alternative is to compare the present results to the CFD predictions obtained at ISL (9). Table 4 shows a summary of the force and moment coefficients, the jet thrust and JI force and moments and the amplification factors. Since the missile is at $\alpha = 0^\circ$, only the axial force coefficient should be non-zero for the no-jet case and the present prediction compares very well (<2%) with that obtained at ISL. For the jet cases, the coefficients also compare reasonably well, within about 10%. Note that the K_m values listed in Table V found in reference 9 appear to be based on a jet location of $X/D = 4.3$, rather than 4.2 for the ISL model. The numbers for the ISL values have been modified in table 4 to use $X/D = 4.2$. In both cases, the center of gravity, or MRP, is assumed to be the same location as the jet nozzle axis and equation 4 is used to calculate K_m .

Table 4. Summary of force and moment validation data, MBL turbulence model, $M = 3.0$, $\alpha = 0^\circ$, PR = 97.

Case	PR	C_{A0}	C_N	$C_{m(0)}$	F_j	F_{ji}	$M_{ji(0)}$	M_{ji}	X_{cp}	X_{cp}/D	K_f	K_m
—	—	—	—	—	[N]	[N]	[N-m]	[N-m]	[m]	—	—	—
ISL CFD	NJ	0.2737	0.0002	-0.0033	—	—	—	—	—	—	—	—
ISL CFD	50	0.2608	0.0800	-0.6281	-15.2	12.3	-3.8768	-1.8104	0.3152	7.88	0.19	3.98 ^a
ISL CFD	70	0.2588	0.0953	-0.7465	-21.4	14.7	-4.6082	-2.1386	0.3135	7.84	0.31	3.50 ^a
ISL CFD	97	0.2563	0.1123	-0.8798	-29.6	17.3	-5.4306	-2.5242	0.3139	7.85	0.42	3.13 ^a
—	—	—	—	—	—	—	—	—	—	—	—	—
ARL CFD	NJ	0.2694	-0.0008	0.0067	—	—	—	—	—	—	—	—
ARL CFD	50	0.2563	0.0750	-0.5859	-14.7	11.6	-3.6161	-1.6718	0.3125	7.81	0.22	3.83
ARL CFD	70	0.2539	0.0884	-0.6885	-20.5	13.6	-4.2490	-1.9571	0.3115	7.79	0.33	3.39
ARL CFD	97	0.2513	0.1029	-0.7976	-28.2	15.9	-4.9226	-2.2549	0.3100	7.75	0.44	3.00

^aValues corrected for $X/D = 4.2$.

3.2 DLR Model

3.2.1 Validation Results

Additional validation data was available using the DLR model, which also included non-zero angle of attack and data with 2 and 3 jets located in the same axial plane (10–13). Figure 12 shows Mach contours on the symmetry and exit planes and C_p contours on the missile surfaces for the 1-, 2-, and 3-jet cases and $-10^\circ \leq \alpha \leq 15^\circ$. The size and strength of the high-pressure region ahead of the jet and the low-pressure region behind the jet increase as the number of jet nozzles increase, as might be expected. The jet flow interactions are also significantly affected by the angle of attack of the missile.

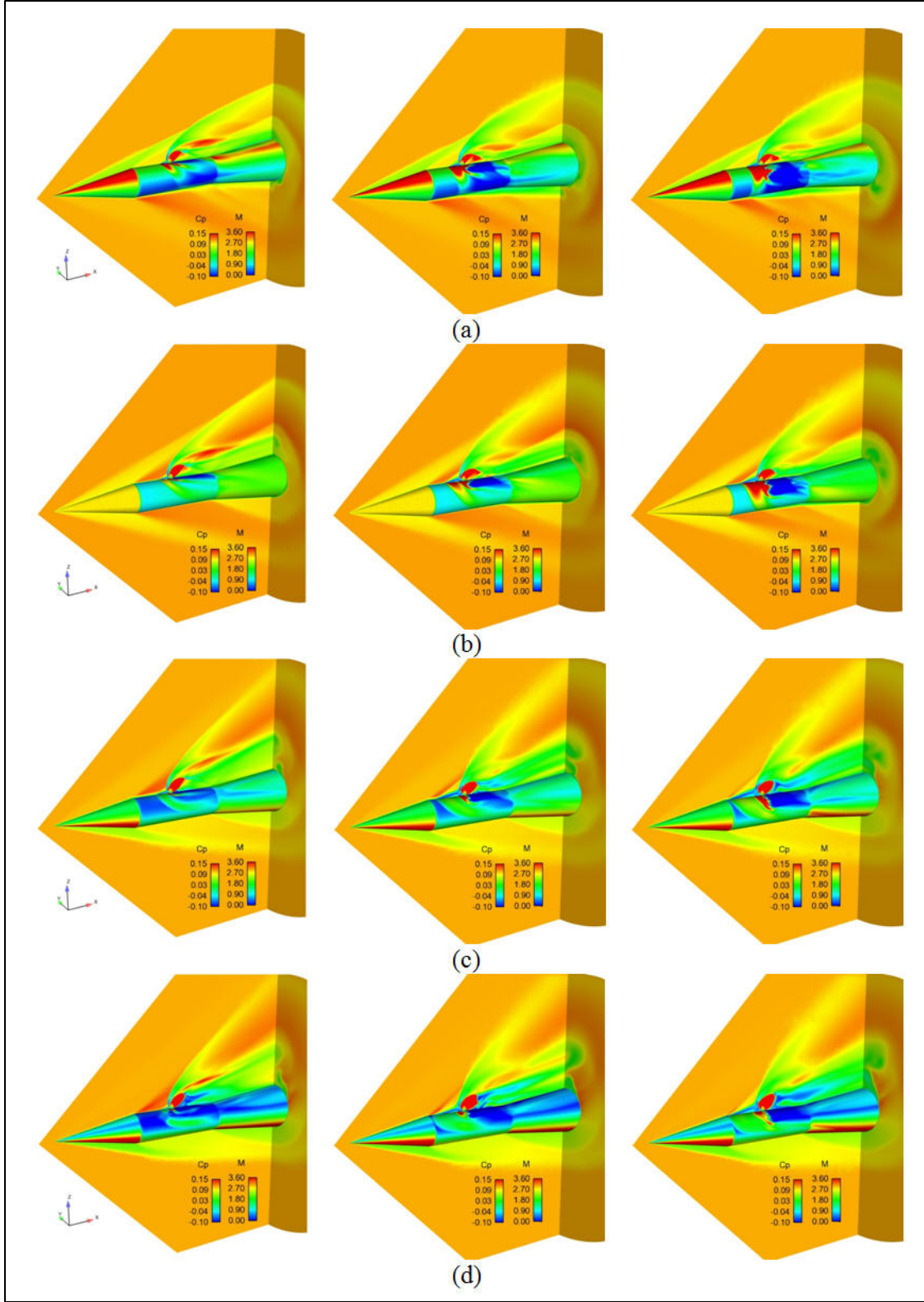


Figure 12. Mach contours on symmetry and exit planes and C_p on missile surfaces for 1- (left), 2- (middle), and 3-jet (right) configurations; (a) $\alpha = -10^\circ$, (b) $\alpha = 0^\circ$, (c) $\alpha = 10^\circ$, and (d) $\alpha = 15^\circ$, $M = 3.0$, $PR = 150$ ($-0.10 \leq C_p \leq 0.15$; $0 \leq M \leq 3.6$).

Figures 13–21 show the comparisons of the current CFD predictions with experimental wind tunnel data from DLR. The x -scale in these figures is the actual nondimensional, axial location along the missile. These data were digitized by the author from Gnemmi et al., 2008 (10), Gnemmi et al., 2006 (11), and Stahl et al., 2008 (12). All CFD data are predictions using the MBL turbulence model. In general, the agreement of the current predictions with the data was very good to excellent. Note that the experimental longitudinal pressure profiles extend much further from the jet nozzle in this case and the prediction of the downstream flow can now be compared. Figure 13 shows the comparison of the longitudinal C_p profiles in line with the jet nozzle ($\phi = 180^\circ$) at Mach 2.8 for the single-jet case with $PR = 100$ and $-10^\circ \leq \alpha \leq 10^\circ$. At each α , the shapes of the pressure profiles are matched very well. The low-pressure region behind the jet is overpredicted slightly from about $X/D = 5$ to 6.5 , but in general the agreement is excellent. Figures 14 and 15 show the longitudinal C_p profiles at locations azimuthally off-set from the jet nozzle, at $\phi = 150^\circ$ and 120° , respectively. The agreement is again excellent.

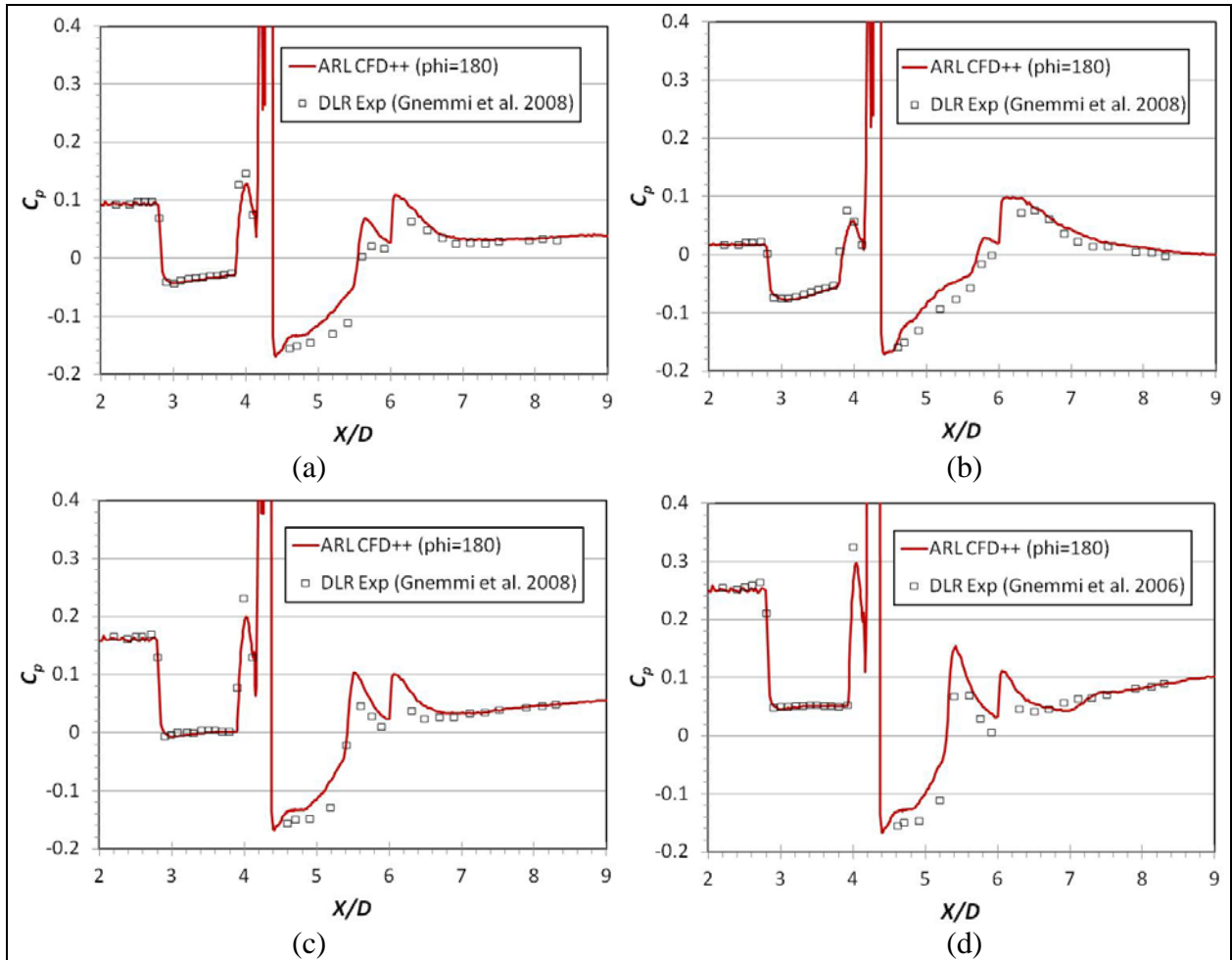


Figure 13. Comparison of predicted and experimental longitudinal C_p profiles at (a) $\alpha = 0^\circ$, (b) $\alpha = 10^\circ$, (c) $\alpha = -5^\circ$, and (d) $\alpha = -10^\circ$ for single-jet case; $M = 2.8$, $PR = 100$, $\phi = 180^\circ$.

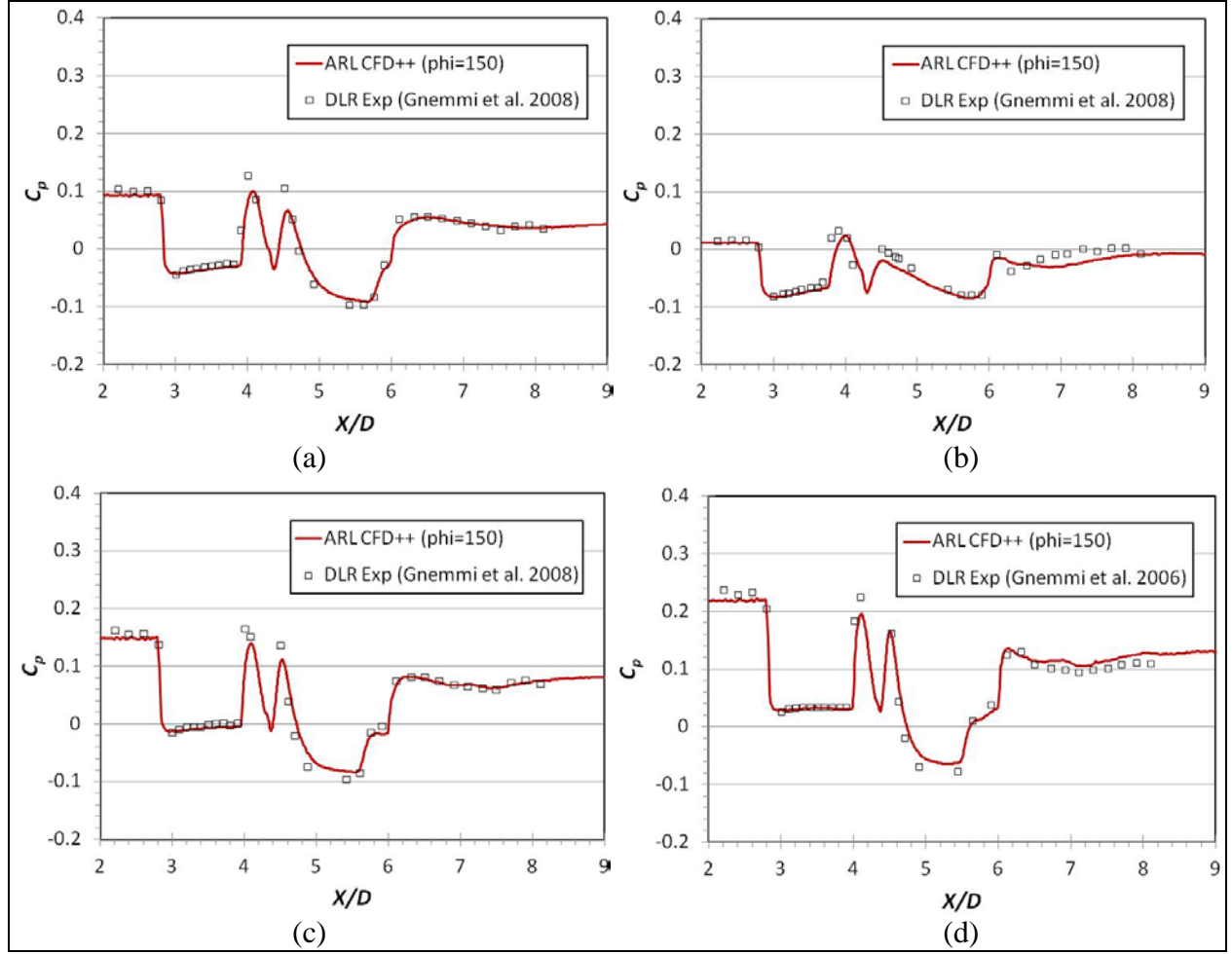


Figure 14. Comparison of predicted and experimental longitudinal C_p profiles at (a) $\alpha = 0^\circ$, (b) $\alpha = 10^\circ$, (c) $\alpha = -5^\circ$, and (d) $\alpha = -10^\circ$, $M = 2.8$ for single-jet case; $PR = 100$, $\phi = 150^\circ$.

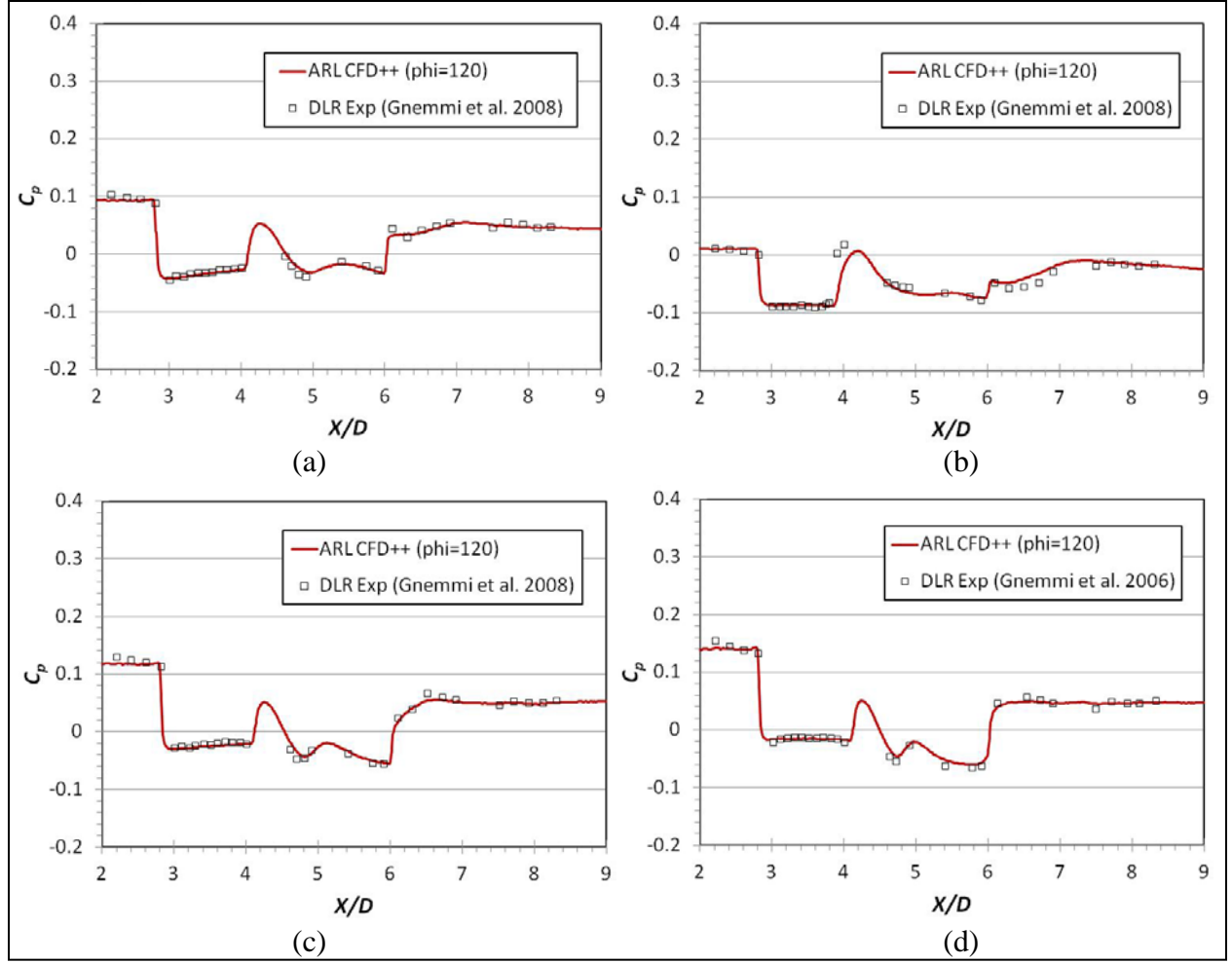


Figure 15. Comparison of predicted and experimental longitudinal C_p profiles at (a) $\alpha = 0^\circ$, (b) $\alpha = 10^\circ$, (c) $\alpha = -5^\circ$, and (d) $\alpha = -10^\circ$ for single-jet case; $M = 2.8$, $PR = 100$, $\phi = 120^\circ$.

Figure 16 shows the comparison of predicted and experimental azimuthal C_p profiles for $\alpha = 0^\circ$ (left), $\alpha = 10^\circ$ (middle), and $\alpha = -10^\circ$ (right) at four axial locations. Again, the agreement is considered excellent. The agreement of the azimuthal profiles (figure 16) and the longitudinal profiles at offset azimuthal locations (figures 14 and 15) are dependent on the accuracy of the prediction of the separation region ahead of the jet (e.g., see figures 13, $2 \leq X/D \leq 4.2$) because the shockwaves and vortices emanate from this region and curve around the body as they move downstream. The prediction of the region ahead of the jet is excellent, leading to excellent predictions of the downstream pressures.

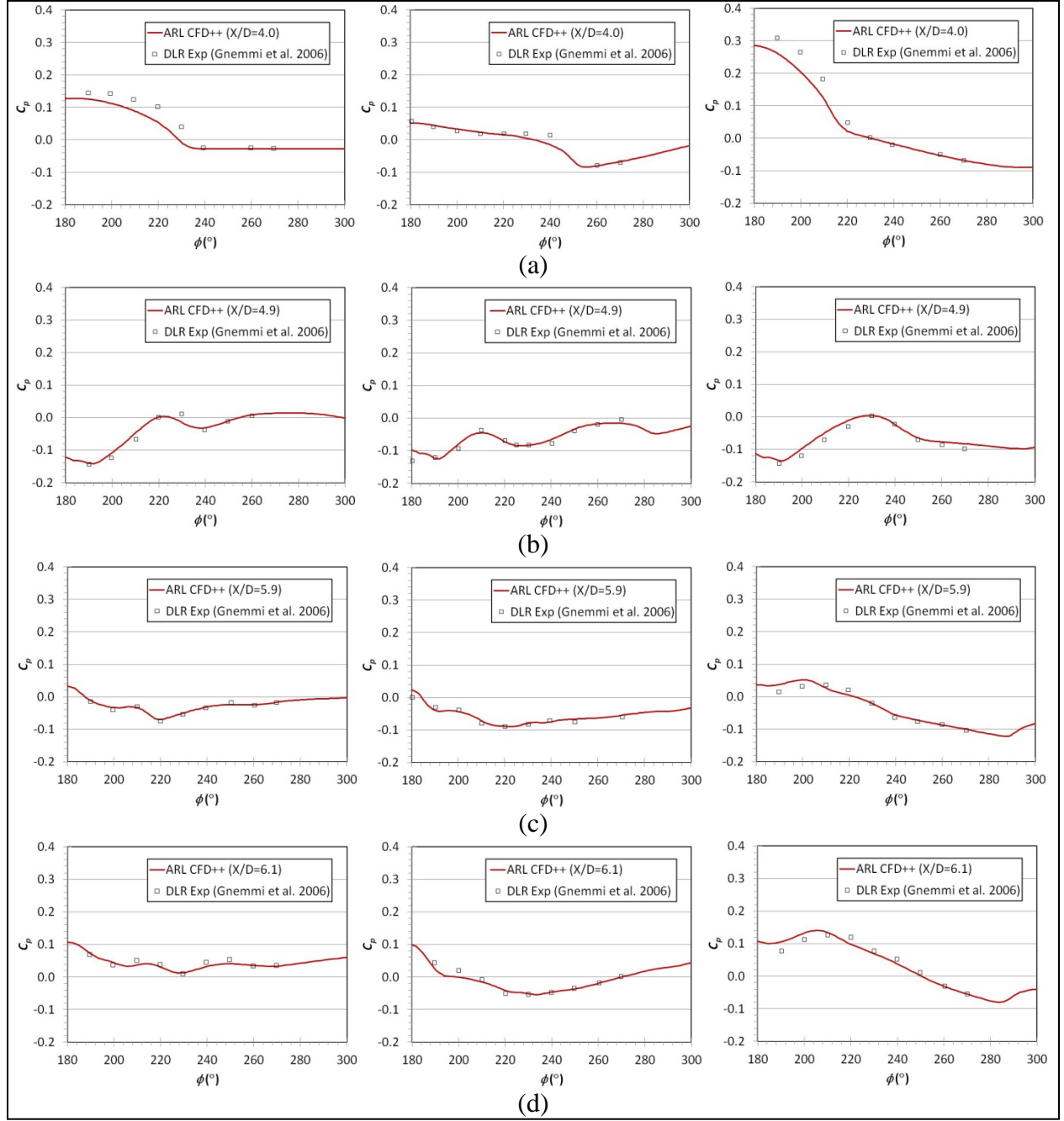


Figure 16. Comparison of predicted and experimental azimuthal C_p profiles for $\alpha = 0^\circ$ (left), $\alpha = 10^\circ$ (middle), and $\alpha = -10^\circ$ (right) at (a) $X/D = 4.0$, (b) $X/D = 4.9$, (c) $X/D = 5.9$, and (d) $X/D = 6.1$ for single-jet case; $M = 2.8$, $PR = 100$.

Figures 17–21 show comparisons of the CFD predictions with experimental data at Mach 3.0. The data from Stahl et al. (12) are presented in terms of $\Delta C_p = C_p - C_{p_{no-jet}}$ and the data is presented as ΔC_p in the figures, resulting in a slightly different profile shape than in the previous figures. Figure 17 shows the comparison of the predicted and experimental longitudinal ΔC_p profiles at $PR = 200$ and four azimuthal locations at $\alpha = 0^\circ$. The predictions are very good, with

again some overprediction of the surface pressure in the plane of the jet ($\phi = 180^\circ$) behind the jet. Figure 18 shows the comparisons at $\phi = 180^\circ$ for the four jet pressure ratios investigated with again very good prediction of the pressure profiles. The over prediction of the downstream pressure peak generally increases with jet pressure ratio.

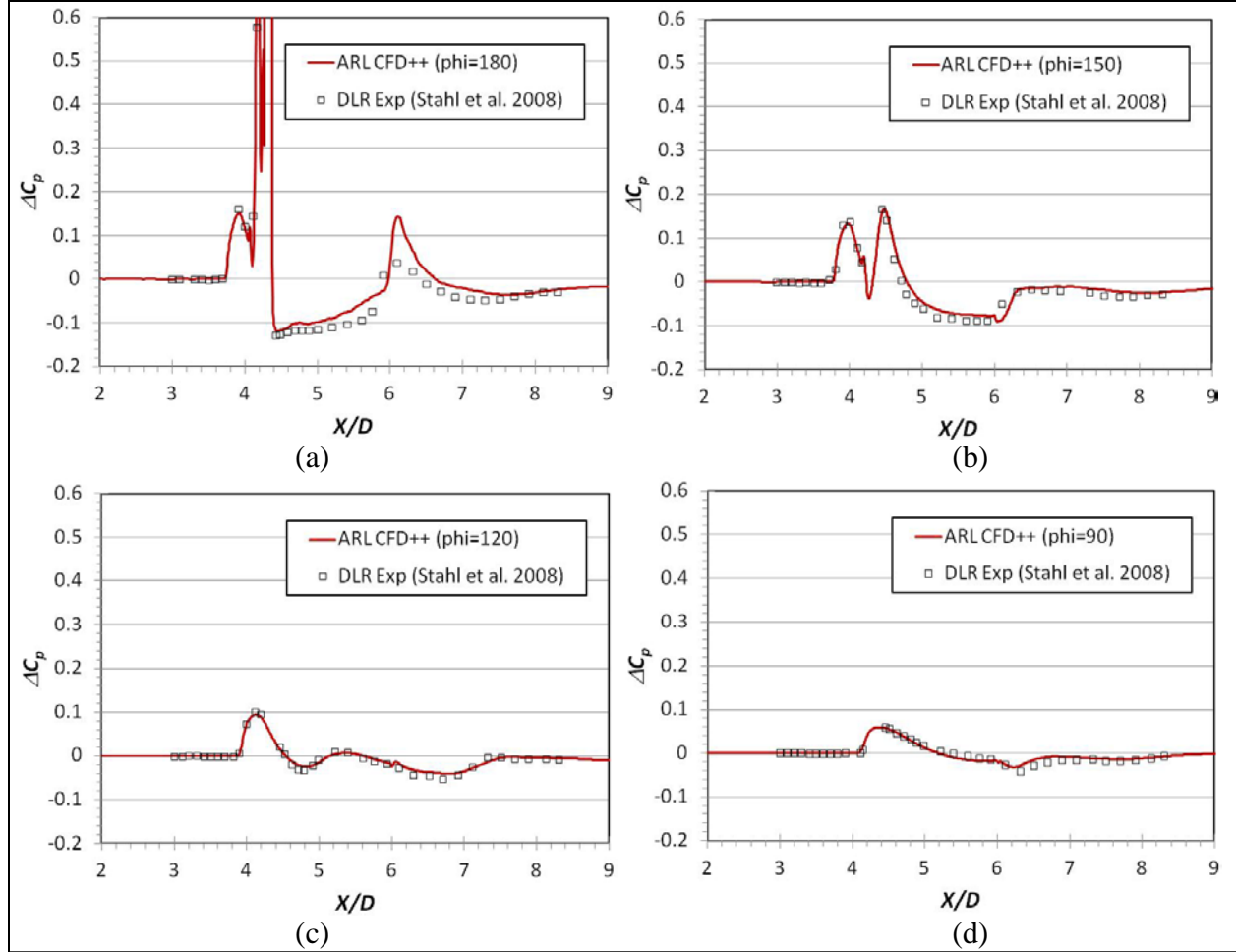


Figure 17. Comparison of predicted and experimental longitudinal ΔC_p profiles at (a) $\phi = 180^\circ$, (b) $\phi = 150^\circ$, (c) $\phi = 120^\circ$, and (d) $\phi = 90^\circ$ for single-jet case; $M = 3.0$, $PR = 200$, $\alpha = 0^\circ$.

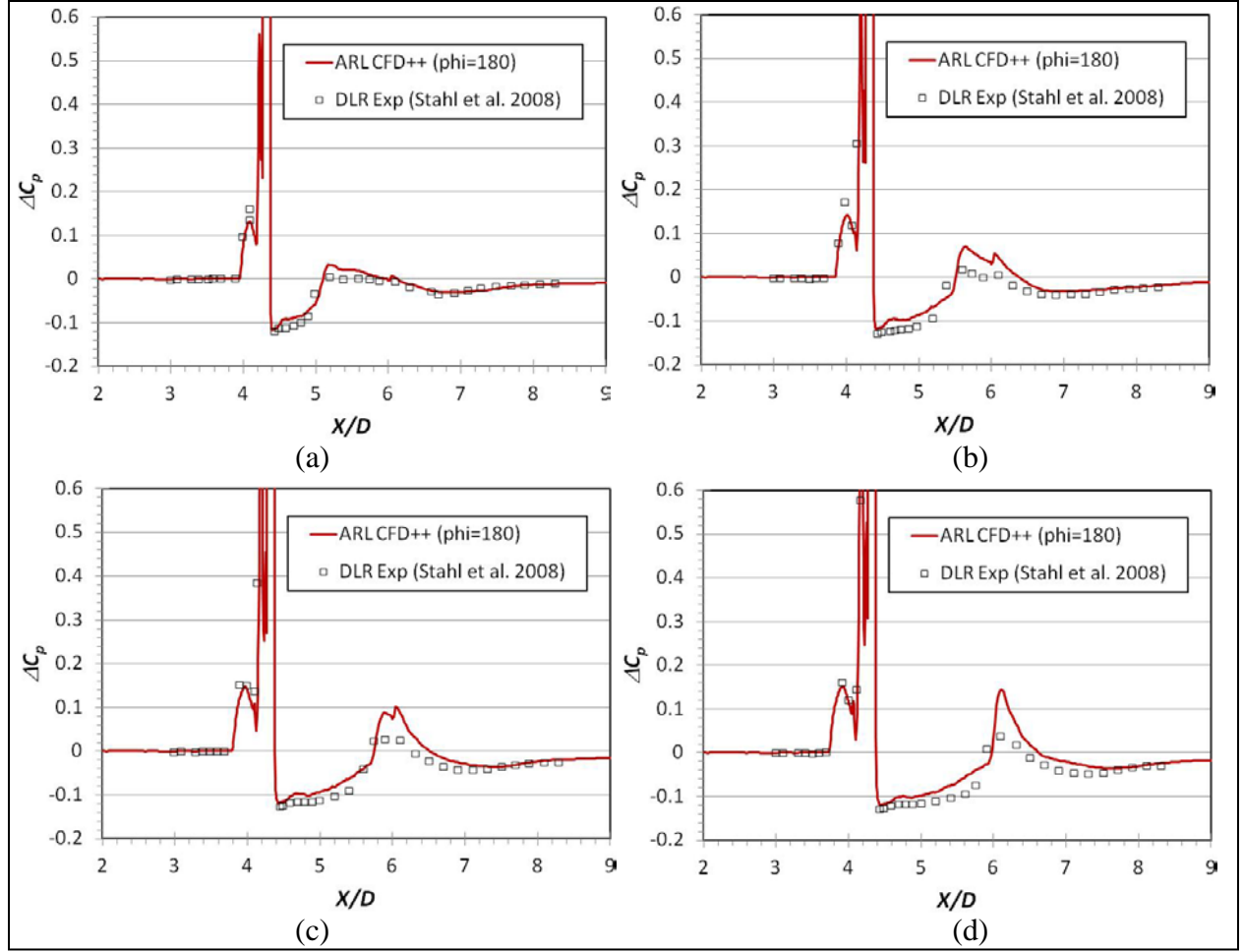


Figure 18. Comparison of predicted and experimental longitudinal ΔC_p profiles at (a) PR = 55, (b) PR = 110, (c) PR = 150, and (d) PR = 200 for single-jet case; $M = 3.0$, $\phi = 180^\circ$, $\alpha = 0^\circ$.

Figures 19–21 show the comparison of predicted and experimental longitudinal ΔC_p profiles at $\phi = 180^\circ$ for $-10^\circ \leq \alpha \leq 15^\circ$ and PR = 150 in the 1-, 2-, and 3-jet configurations. The single-jet case predictions compare very well with the experimental data at all α . The downstream pressure profile prediction improves at positive α , as the jet plume moves farther from the projectile and the pressure is reduced (e.g., see figure 12). The predictions of ΔC_p for the 2- and 3-jet configurations do not compare quite as well with experimental data in the separation region ahead of the jet. Generally, the prediction of the onset of the separation zone is predicted to occur slightly further downstream, but the peak pressures are predicted reasonably accurately. The downstream pressure profiles are generally well predicted. The mesh density boxes were widened to accommodate the additional jet nozzles when making the new meshes; however, an additional mesh sensitivity study was not performed for these cases. The jet near-field mesh density is still believed to be adequate.

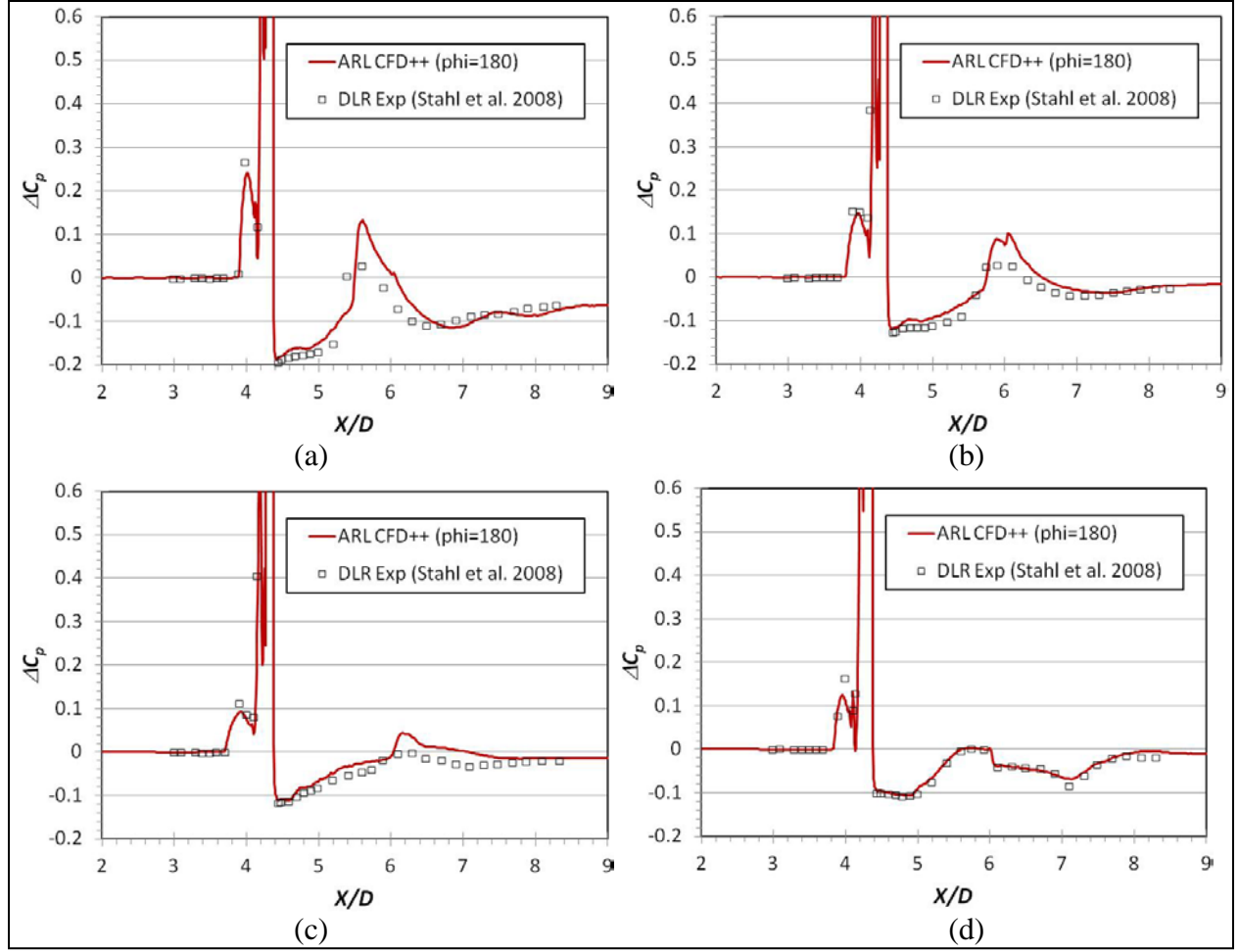


Figure 19. Comparison of predicted and experimental longitudinal ΔC_p profiles at (a) $\alpha = -10^\circ$, (b) $\alpha = 0^\circ$, (c) $\alpha = 10^\circ$, and (d) $\alpha = 15^\circ$ for single-jet case; $M = 3.0$, $\phi = 180^\circ$, $PR = 150$.

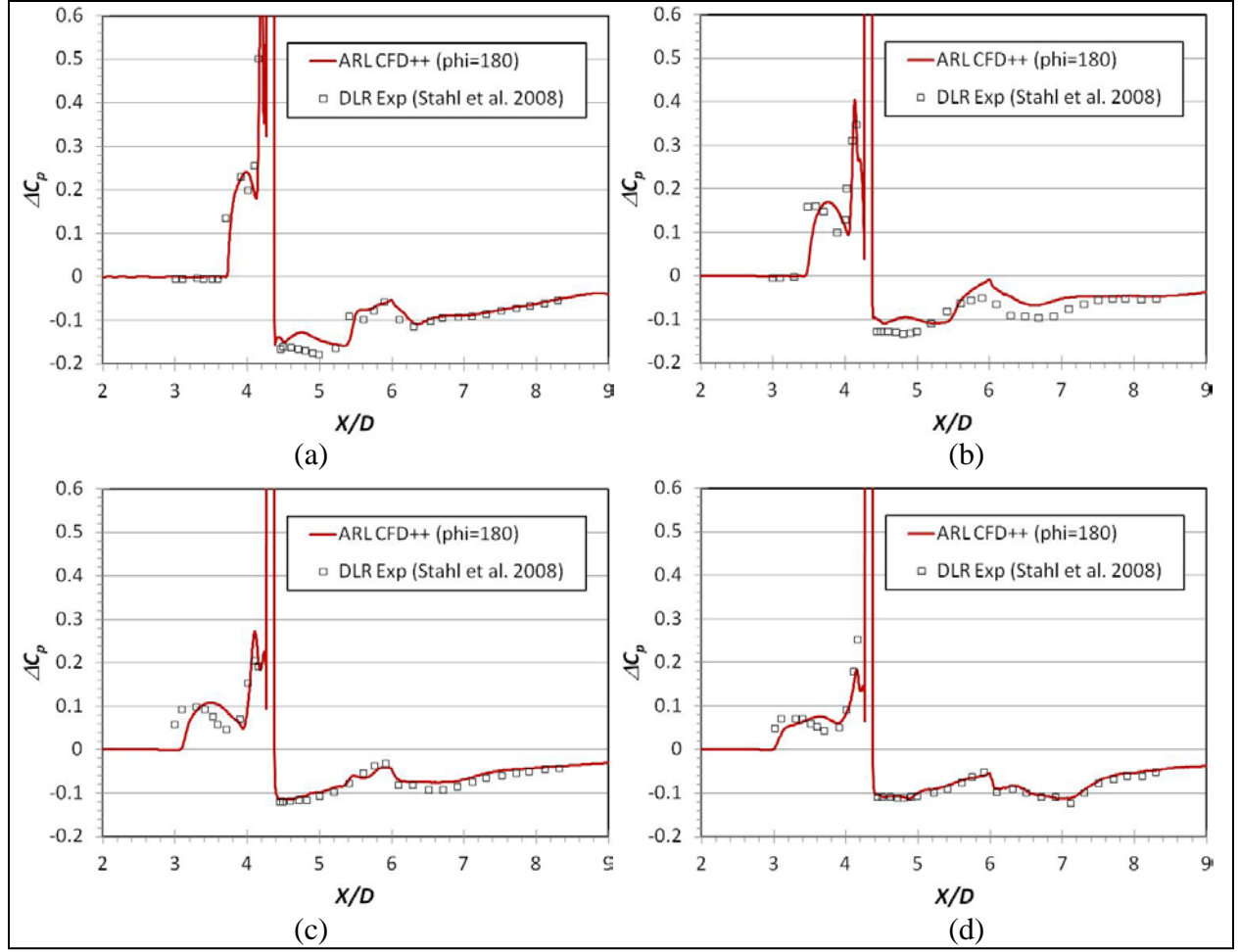


Figure 20. Comparison of predicted and experimental longitudinal ΔC_p profiles at (a) $\alpha = -10^\circ$, (b) $\alpha = 0^\circ$, (c) $\alpha = 10^\circ$, and (d) $\alpha = 15^\circ$ for 2-jet case; $M = 3.0$, $\phi = 180^\circ$, PR = 150.

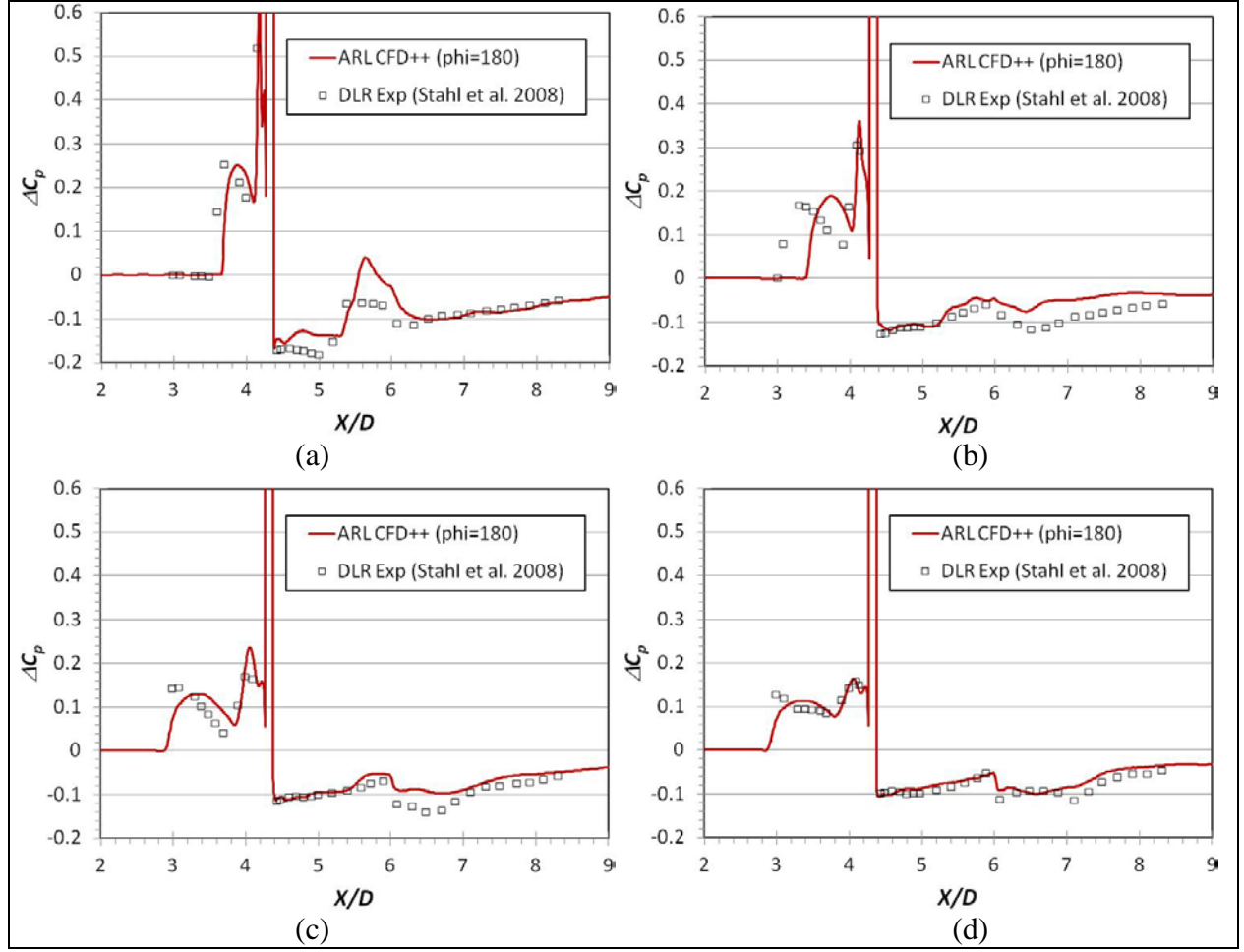


Figure 21. Comparison of predicted and experimental longitudinal ΔC_p profiles at (a) $\alpha = -10^\circ$, (b) $\alpha = 0^\circ$, (c) $\alpha = 10^\circ$, and (d) $\alpha = 15^\circ$ for 3-jet case; $M = 3.0$, $\phi = 180^\circ$, $PR = 150$.

3.2.2 Comparison With ISL CFD With DLR Model

Table 5 shows a summary of the ARL CFD predictions of the DLR model at Mach 2.8 using the MBL turbulence model. Data for the no-jet ($PR = 0$) case and with a jet at $PR = 100$ are shown. These data are compared to the results from ISL for the same model (11) in table 6. The predicted force and moment data compare reasonably well. Note that the axial force, F_A , data presented in reference 11, and shown in red in table 6, is much higher than the ARL predictions. Like the ARL simulations, the ISL simulations did not include a solution of the missile base flow, so the reason for the discrepancy is not understood. Also, the ISL predicted moment data for the jet case at $\alpha = -5^\circ$ is much lower than expected, considering the predicted J_I force compares very well to the ARL prediction. The ISL predicted force amplification factor, K_f , is also lower than the current predictions by 0.13–0.21 across the angle of attack range.

Table 5. Summary of ARL CFD predicted force and moment data, MBL TM, $M = 2.8$.

α	PR	F_j	F_{A0}	F_{ji}	$M_{ji(0)}$	M_{ji}	X_{cp}/D	K_f	K_m
[°]		[N]	[N]	[N]	[N-m]	[N-m]	—	—	—
-10	0	—	31.10	-170.76	34.994	5.623	5.12	—	—
—	100	-28.4	28.18	-148.27	28.333	2.829	4.78	0.21	3.46
-5	0	—	34.92	-69.21	13.549	1.644	4.89	—	—
—	100	-28.4	32.27	-52.46	8.573	-0.450	4.09	0.41	2.84
0	0	—	36.37	-0.08	0.023	0.008	6.76	—	—
—	100	-28.4	33.95	14.34	-4.312	-1.846	7.52	0.49	2.63
10	0	—	31.09	170.42	-34.890	-5.578	5.12	—	—
—	100	-28.4	30.96	176.29	-37.201	-6.880	5.28	0.79	2.14

Table 6. Summary of ISL CFD (II) predicted force and moment data, SST TM, $M = 2.8$.

a	PR	F_j	F_A	F_i	$M_{i(0)}$	M_i	X_{cp}/D	K_f	K_m
[°]		[N]	[N]	[N]	[N-m]	[N-m]	—	—	—
-10	0	—	104.36	-171.32	35.142	5.675	5.13	—	—
—	100	-26.1	101.72	-145.20	27.533	2.559	4.74	0.00	3.99
-5	0	—	108.50	-68.72	13.388	1.568	4.87	—	—
—	100	-26.1	106.10	-47.94	3.663	-4.583	1.91	0.20	6.89
0	0	—	110.02	0.54	-0.196	-0.103	9.07	—	—
—	100	-26.1	107.68	17.36	-5.182	-2.196	7.46	0.36	3.00
10	0	—	105.08	176.38	-35.995	-5.658	5.10	—	—
—	100	-26.1	104.80	178.24	-37.903	-7.246	5.32	0.93	2.52

3.2.3 Turbulence Model Effects on DLR Model Results

The same nine turbulence models compared in section 3.1.2 are again compared here using the DLR model at Mach 3.0, PR = 200, $\alpha = 0^\circ$, and $\alpha = 10^\circ$. Again, the default parameters for each turbulence model were not varied and the free shear flow-based compressibility correction was used. Figure 22 shows the comparison of the k - ω -based models. All models perform reasonably well, but the MBL and kw models predict the pressure best over the whole profile at azimuthal locations less than 180° . Comparing the k - ε -based models, figure 23, shows that the keR model performs the best, nearly matching the MBL model results. Comparing the SA and SARC models, figure 24, the SA model again predicts the pressure profiles very well, closely matching the MBL model. The SARC model matches the experimental data better than the SA and MBL models at $\phi = 90^\circ$, but this may be a coincidence from the SARC model under predicting the onset of the forward separation region. These same models (MBL, kw, keR, SA) also perform the best in predicting the pressure profiles at $\alpha = 10^\circ$, as shown in figure 25.

The variation of the predicted forces and moments due to turbulence model are very low. The data for $\alpha = 0^\circ$ and $\alpha = 10^\circ$ are compared in tables 7 and 8, respectively. The variation of the JI forces and moments are less than 4% for $\alpha = 0^\circ$ and less than 2% for $\alpha = 10^\circ$. Like the results for the ISL configuration, table 3, these variations are within the expected accuracy of most CFD predictions.

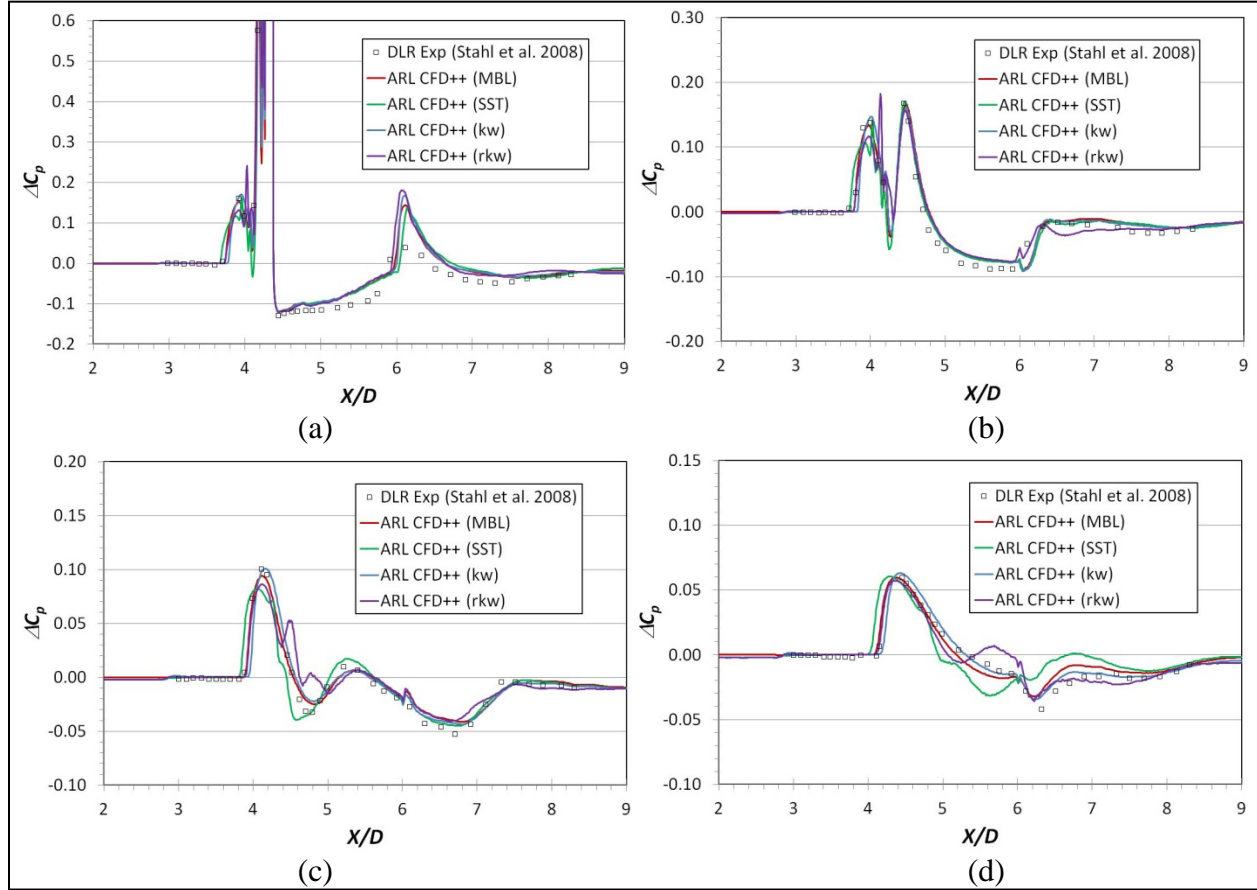


Figure 22. Effect of $k-\omega$ -based turbulence models on 1-jet DLR case: $M = 3.0$, $PR = 200$, $\alpha = 0^\circ$, and (a) $\phi = 180^\circ$, (b) $\phi = 150^\circ$, (c) $\phi = 120^\circ$, and (d) $\phi = 90^\circ$.

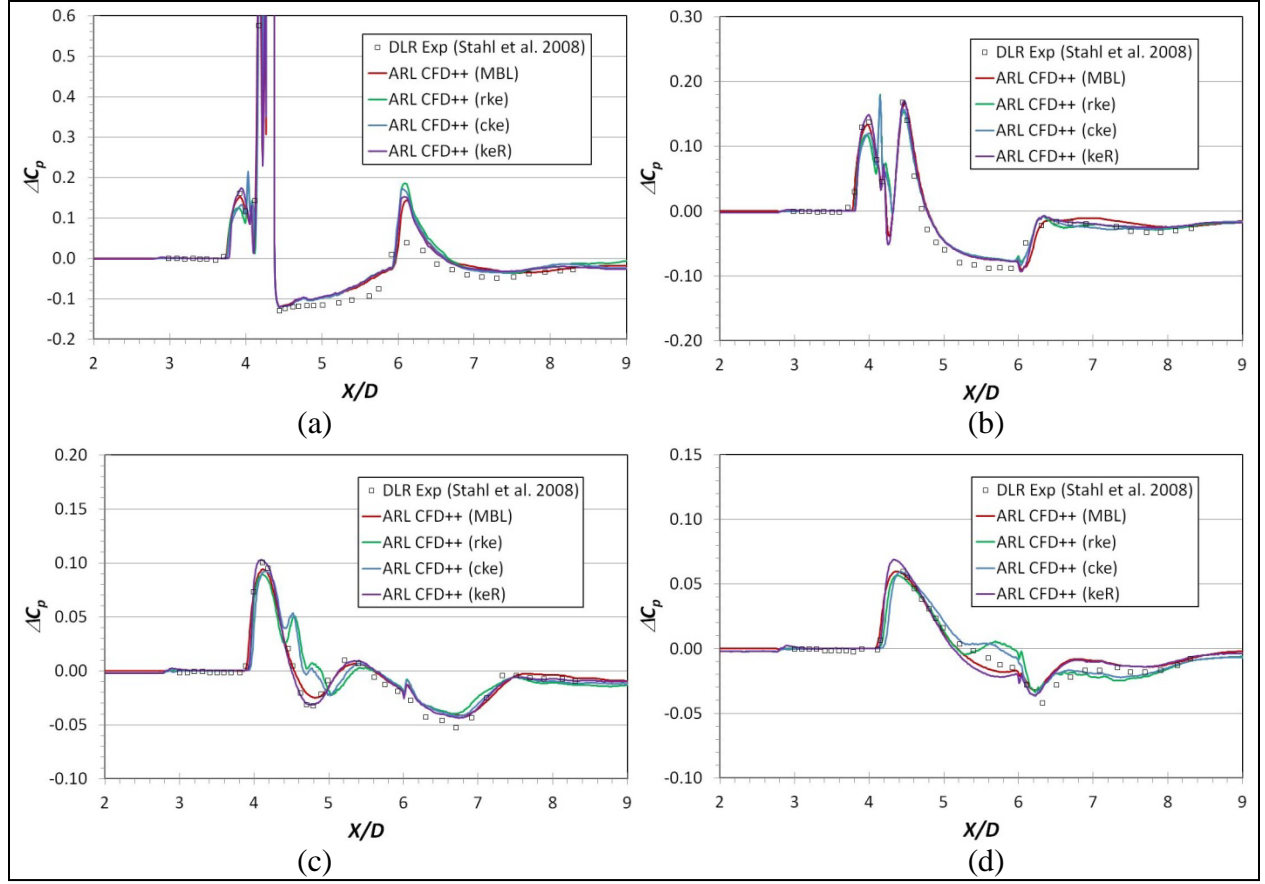


Figure 23. Effect of MBL and k - ε -based turbulence models on 1-jet DLR case: $M = 3.0$, $PR = 200$, $\alpha = 0^\circ$, and (a) $\phi = 180^\circ$, (b) $\phi = 150^\circ$, (c) $\phi = 120^\circ$, and (d) $\phi = 90^\circ$.

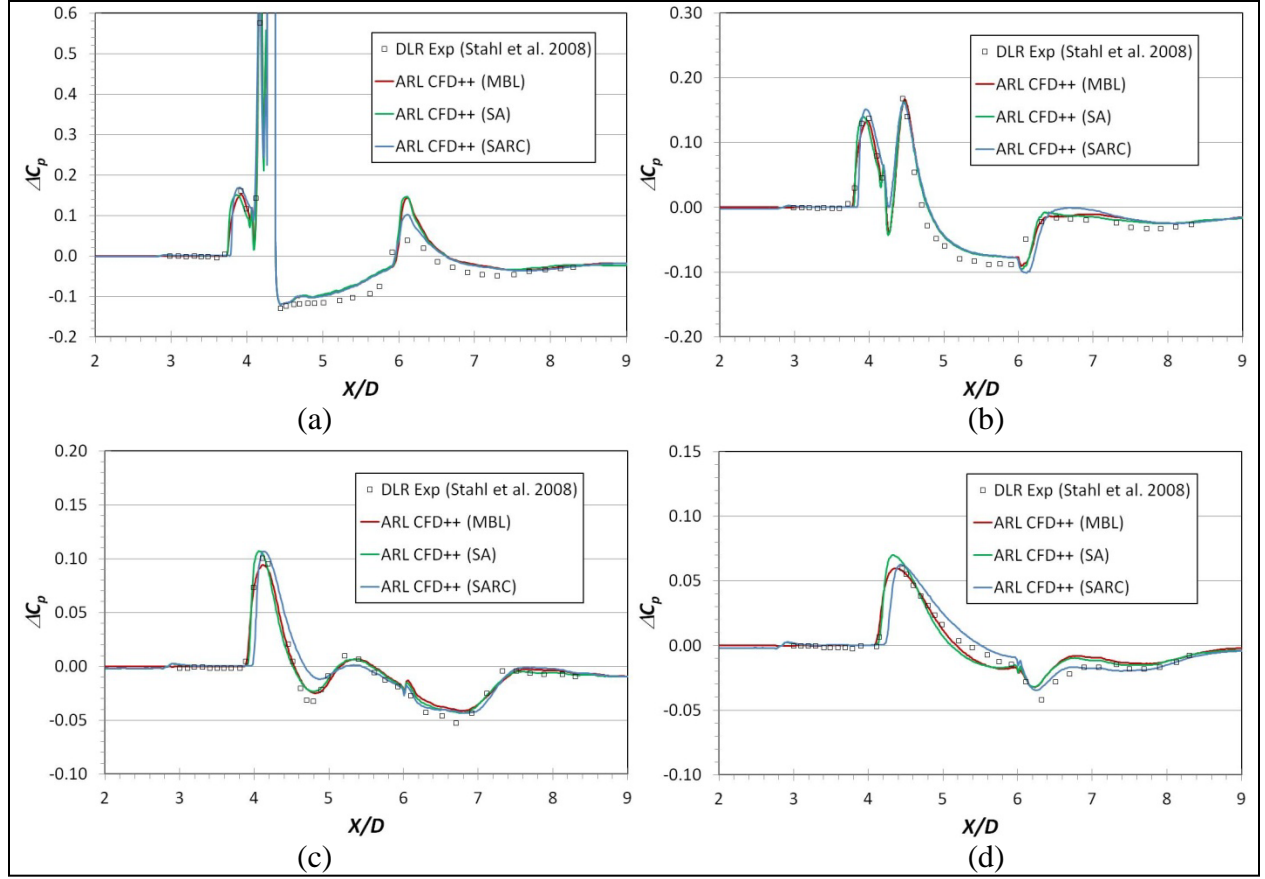


Figure 24. Effect of MBL and SA-based turbulence models on 1-jet DLR case: $M = 3.0$, $PR = 200$, $\alpha = 0^\circ$, and (a) $\phi = 180^\circ$, (b) $\phi = 150^\circ$, (c) $\phi = 120^\circ$, and (d) $\phi = 90^\circ$.

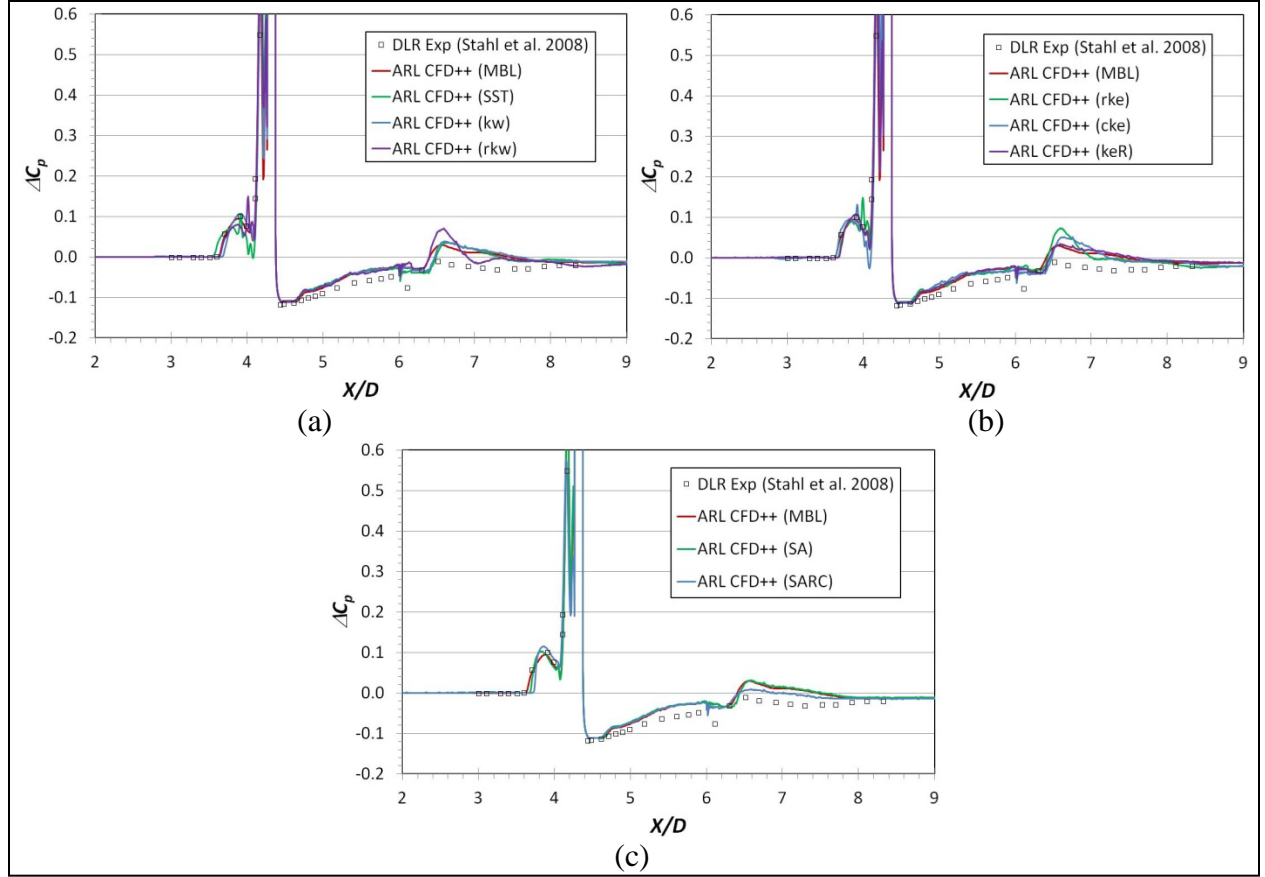


Figure 25. Effect of (a) k - ω -based, (b) MBL and k - ε -based, and (c) MBL and SA-based turbulence models on 1-jet DLR case $M = 3.0$, $PR = 200$, $\phi = 180^\circ$, and $\alpha = 10^\circ$.

The MBL model provided the most accurate prediction of the pressure profiles for both the ISL and DLR configurations. However, it is interesting to note that the rkW and cke models performed better at predicting the pressure profiles in the ISL configuration, while the kw and keR models performed better in the DLR configuration. This may indicate that these are perhaps subtle differences, which is reinforced by the small variation in the integrated forces and moments shown in tables 7 and 8. However, some of the turbulence models in this study predicted some significant differences in surface pressure and separation region length. These differences could lead to variation in strength and location of the CVP, which could lead to different JI forces and moments due to interaction with tail fins or other downstream appendages that might be present on a munition.

Table 7. Summary of turbulence model effects, $M = 3.0$, $PR = 200$, $\alpha = 0^\circ$ ($F_j = -42.8$ N).

TM	C_{A0}	C_N	$C_{m(0)}$	F_j	F_{ji}	$M_{ji(0)}$	M_{ji}	X_{cp}	X_{cp}/D	K_f	K_m
—	—	—	—	[N]	[N]	[N-m]	[N-m]	[m]	—	—	—
MBL	0.2287	0.1240	-0.9618	-42.8	15.4	-4.7832	-2.1306	0.3101	7.75	0.64	2.25
SST	0.2254	0.1216	-0.9246	-42.8	15.1	-4.5981	-1.9987	0.3043	7.61	0.65	2.17
kw	0.2321	0.1197	-0.9438	-42.8	14.9	-4.6935	-2.1341	0.3154	7.89	0.65	2.25
rkW	0.2292	0.1223	-0.9806	-42.8	15.2	-4.8766	-2.2603	0.3206	8.01	0.64	2.32
SA	0.2343	0.1204	-0.9332	-42.8	15.0	-4.6408	-2.0660	0.3100	7.75	0.65	2.21
SARC	0.2373	0.1234	-0.9676	-42.8	15.3	-4.8121	-2.1741	0.3138	7.84	0.64	2.27
rke	0.2285	0.1154	-0.9301	-42.8	14.3	-4.6254	-2.1577	0.3224	8.06	0.66	2.26
cke	0.2252	0.1191	-0.9632	-42.8	14.8	-4.7901	-2.2424	0.3234	8.08	0.65	2.31
keR	0.2335	0.1195	-0.9286	-42.8	14.9	-4.6178	-2.0617	0.3107	7.77	0.65	2.21
—	—	—	—	—	—	—	—	—	—	—	—
Mean	0.2304	0.1206	-0.9482	-42.8	15.0	-4.7153	-2.1362	0.3145	7.86	0.65	2.25
STD	0.0041	0.0026	0.0205	0.01	0.33	0.1018	0.0851	0.0065	0.16	0.01	0.05
%STD	1.79%	2.17%	-2.16%	-0.03%	2.17%	-2.16%	-3.99%	2.07%	2.07%	1.18%	2.20%

Table 8. Summary of turbulence model effects, $M = 3.0$, $PR = 200$, $\alpha = 10^\circ$.

TM	C_{A0}	C_N	$C_{m(0)}$	F_j	F_{ji}	$M_{ji(0)}$	M_{ji}	X_{cp}	X_{cp}/D	K_f	K_m
—	—	—	—	[N]	[N]	[N-m]	[N-m]	[m]	—	—	—
MBL	0.2136	1.2622	-6.7725	-42.8	156.9	-33.680	-6.6898	0.2146	5.37	0.86	1.86
SST	0.2146	1.2447	-6.6647	-42.8	154.7	-33.144	-6.5270	0.2142	5.35	0.91	1.77
kw	0.2223	1.2582	-6.7483	-42.8	156.4	-33.559	-6.6546	0.2145	5.36	0.87	1.84
rkW	0.2192	1.2275	-6.5792	-42.8	152.6	-32.718	-6.4701	0.2144	5.36	0.96	1.73
SA	0.2267	1.2627	-6.7738	-42.8	157.0	-33.686	-6.6836	0.2146	5.36	0.85	1.86
SARC	0.2297	1.2496	-6.7046	-42.8	155.4	-33.342	-6.6208	0.2146	5.37	0.89	1.82
rke	0.2186	1.2284	-6.5806	-42.8	152.7	-32.725	-6.4575	0.2143	5.36	0.95	1.73
cke	0.2157	1.2386	-6.6325	-42.8	154.0	-32.984	-6.4975	0.2142	5.35	0.92	1.75
keR	0.2268	1.2608	-6.7594	-42.8	156.7	-33.615	-6.6544	0.2145	5.36	0.86	1.84
—	—	—	—	—	—	—	—	—	—	—	—
Mean	0.2208	1.2481	-6.6906	-42.77	155.2	-33.273	-6.5839	0.2144	5.36	0.90	1.80
STD	0.0059	0.0141	0.0794	0.01	1.75	0.3950	0.0949	0.0002	0.00	0.04	0.06
%STD	2.66%	1.13%	-1.19%	-0.03%	1.13%	-1.19%	-1.44%	0.08%	0.08%	4.58%	3.09%

The CVP is illustrated in figure 26, which shows vorticity contours on five axial planes along the missile flare and velocity magnitude contours on the symmetry plane. The vorticity contours and missile body have been mirrored across the symmetry plane, which has also been made transparent for illustration. The effect of the turbulence model on the trajectory of the CVP was estimated by extracting the radial location of the maximum vorticity magnitude on the symmetry plane. This does not provide explicit information on the turbulence model effects on vortex core strength or lateral distance variation of the two cores, but it provides an estimate of the order of the turbulence model effects on the CVP. Figure 27 shows variation of the predicted CVP trajectory with turbulence model as the radial distance away from the missile body, not counting the flared section (i.e., 20 mm was subtracted from actual radial distance). The trajectory was calculated by extracting radial profiles of solution data at eight axial locations aft of the barrel shock on the symmetry plane and calculating the maximum vorticity within each profile. Also shown in the figure are the profile of the missile and the location of the jet nozzle axis. The difference in the trajectory due to turbulence model varies from a minimum of 0.9 mm at $x = 320$ mm to a maximum of 1.6 mm at $x = 280$ mm. Table 9 displays the same data, including the mean and standard deviation, which is less than 6%. In general, there is little variation in the radial location of the CVP with turbulence model.

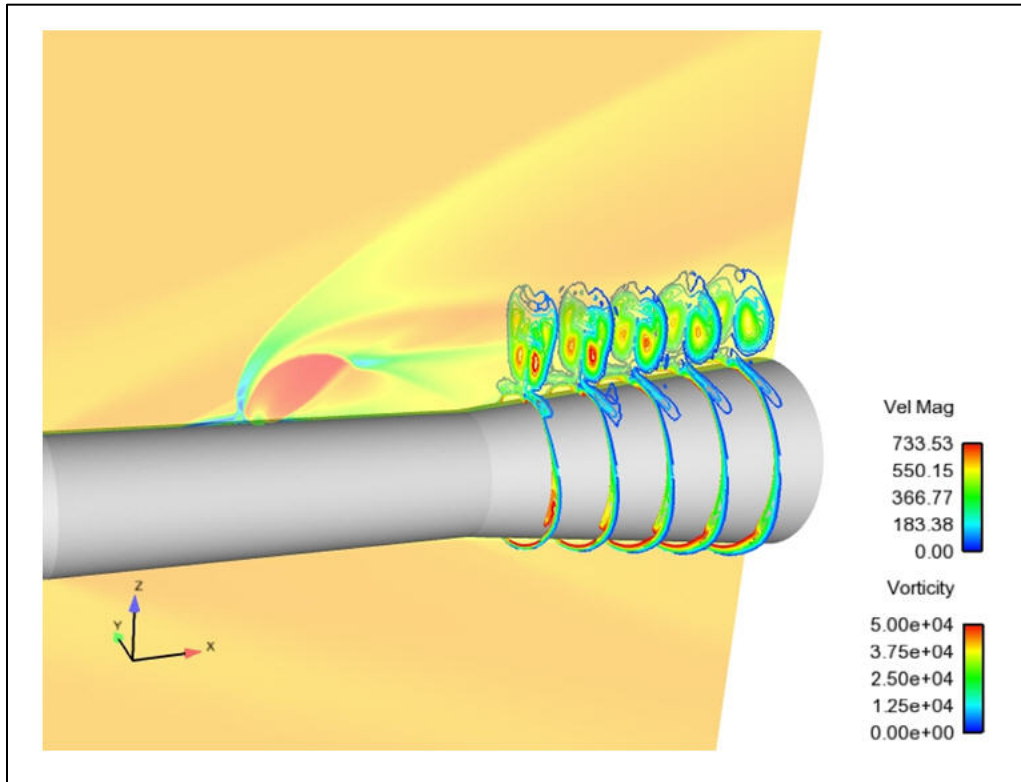


Figure 26. Velocity magnitude contours on symmetry plane and vorticity contours on five axial planes along flare section.

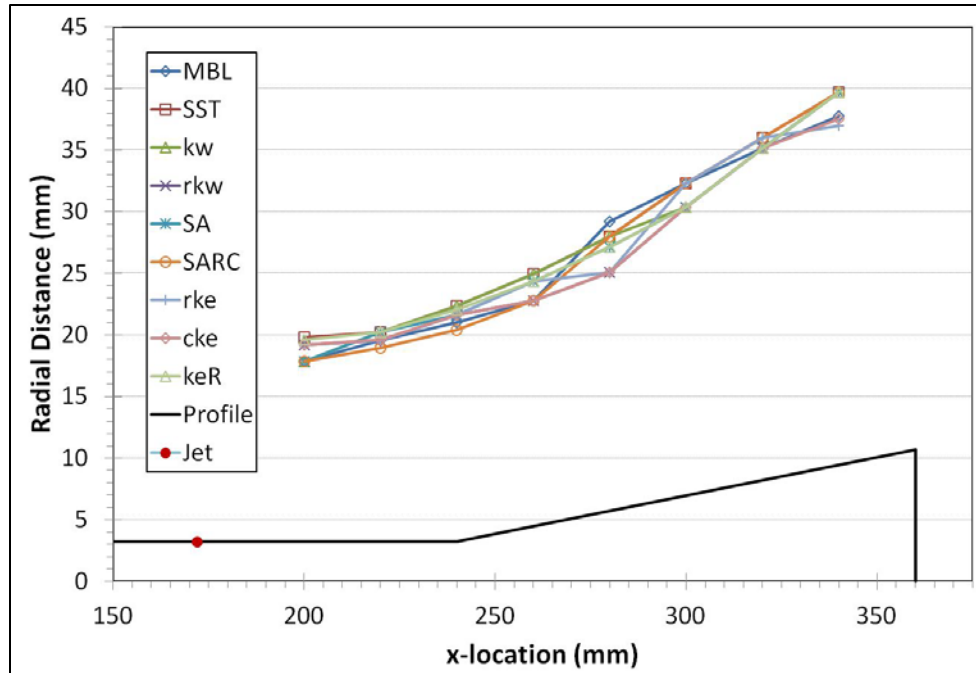


Figure 27. Variation of location of maximum symmetry plane vorticity with missile axial location and turbulence model.

Table 9. Variation of location of maximum symmetry plane vorticity with missile axial location and turbulence model (all distances in mm).

x-loc	MBL	SST	kw	rkw	SA	SARC	rke	cke	keR	Mean	STD	%STD
200	17.8	19.8	17.8	19.2	17.8	17.8	19.2	19.2	19.6	18.7	0.85	4.54
220	19.6	20.2	20.2	19.6	20.2	19.0	19.6	19.6	20.2	19.8	0.44	2.23
240	21.0	22.4	22.4	21.6	21.6	20.4	21.6	21.6	22.0	21.6	0.62	2.86
260	22.8	25.0	25.0	22.8	24.4	22.8	24.4	22.8	24.4	23.8	1.00	4.20
280	29.2	28.0	28.0	25.1	27.1	28.0	25.1	25.1	27.1	27.0	1.55	5.76
300	32.3	32.3	30.4	30.4	30.4	32.3	32.3	30.4	30.4	31.2	1.00	3.22
320	35.1	36.0	35.1	35.1	35.1	36.0	36.0	35.1	35.1	35.4	0.43	1.21
340	37.7	39.7	39.7	39.7	39.7	39.7	37.0	37.5	39.7	38.9	1.16	2.98

Figure 28 shows the variation of the maximum vorticity on the symmetry plane—generated by passage of the CVP—with axial location and turbulence model. There is wide variation in the vorticity closer to the jet, and then the values appear to converge as they travel downstream. However, there is a fairly wide variation of maximum vorticity in the far-downstream locations, as shown in table 10, where the percent standard deviation is about 28%–37%. The large variation at the first location, $x = 200$ mm, can be due to the small differences in predicting the near-field jet structure. The barrel shock and Mach disk are likely impacting the CVP at this first location. Summarizing, while there is little effect of turbulence model on the trajectory of the CVP, there is a significant effect on the vortex intensity. These differences in vorticity on the

symmetry plane can be due to variations in vortex intensity within the CVP, lateral separation of the two vortices or some combination of both. These variations could be important in predicting the forces and moments on a missile with tail-mounted fins, because the vortex intensity of the CVP as it passes near the fins will affect the surface pressure distribution, and thus the predicted resultant forces and moment.

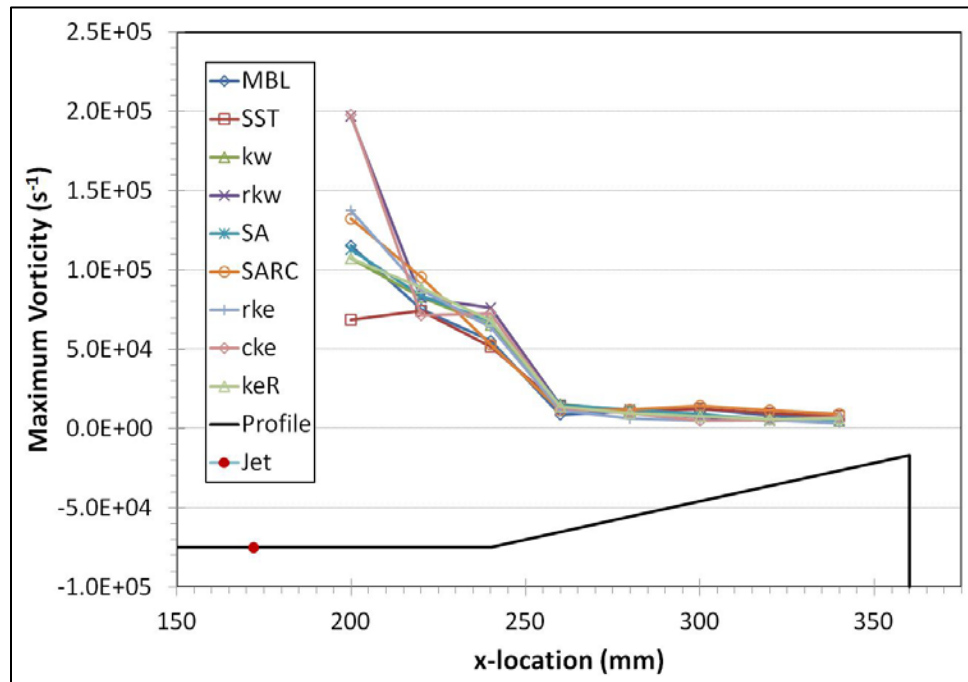


Figure 28. Variation of maximum vorticity with missile axial location and turbulence model.

Table 10. Variation of maximum vorticity with missile axial location and turbulence model.

x-loc	Mean	STD	%STD
(mm)	(s ⁻¹)	(s ⁻¹)	%
200	1.3E+05	4.3E+04	32.5
220	8.3E+04	7.7E+03	9.3
240	6.4E+04	8.6E+03	13.5
260	1.3E+04	2.2E+03	16.8
280	1.0E+04	1.8E+03	17.3
300	9.1E+03	3.4E+03	36.9
320	6.9E+03	2.4E+03	34.1
340	6.1E+03	1.7E+03	28.1

The effects of turbulence model on surface pressure and flow structure are further illustrated in figure 29, which shows C_p contours and simulated surface oil flow patterns on the missile. The features of the pressure contours and surface flow patterns are correlated to the pressure profiles in figures 22–24. There is a separation line well ahead of the jet nozzle and this flow reattaches closer to the nozzle, encompassing the region under the λ -shock (see figure 1). For some turbulence models, the attachment line is farther forward (e.g., the SST, rkw, rke, and cke). These four models show a second pressure peak ahead of the jet nozzle in figures 22 and 24. The forward separation location also varies with the initial pressure rise shown in figures 22–24.

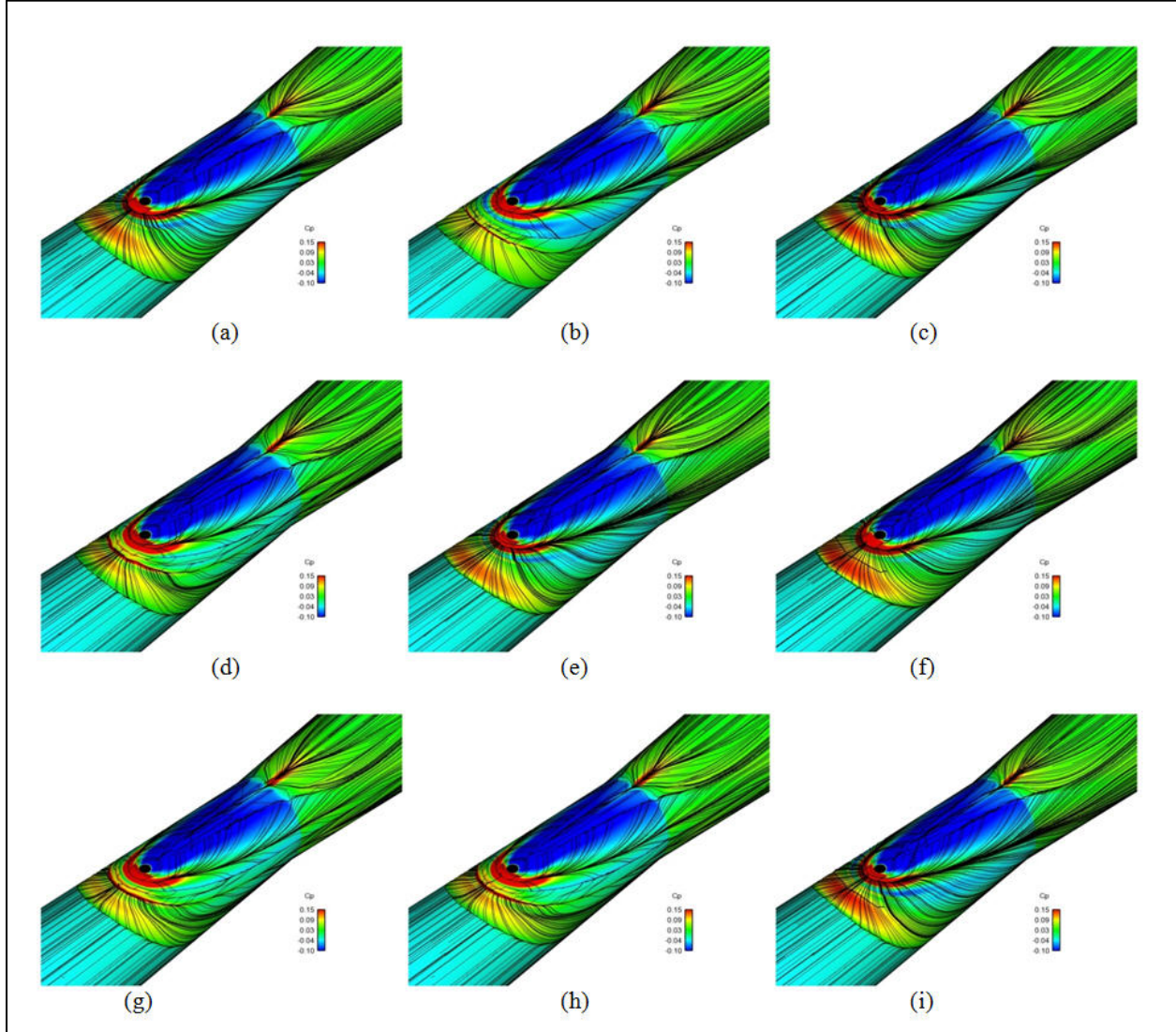


Figure 29. Simulated surface oil flow streamlines and C_p contours ($-0.10 \leq C_p \leq 0.15$) on surface of missile for cases with (a) MBL, (b) SST, (c) kw, (d) rkw, (e) SA, (f) SARC, (g) rke, (h) cke, and (i) keR turbulence models.

Other moderate differences in the surface flow streamlines among the turbulence models can be observed in figure 29. The initial forward separation and attachment lines curve around the missile body as they flow downstream and indicate the location of the horseshoe vortices close to the body. These are illustrated in figure 26 as the regions of high vorticity on the lower section of the flare section of the missile. Therefore, differences in the forward separation and attachment locations lead to differences in strength and location of horseshoe vortices.

Another set of separation and attachment lines are observed in figure 29 behind the jet nozzle, in the wake of the jet. A node of attachment is located at the end of the separation region behind the nozzle, indicated by the high pressure and the point from which the flow streamlines emerge. The wake vortices travel close to the surface in this region and are illustrated in figure 26 as the vortices directly under the CVP. There appears to be less variation with turbulence model in this wake region directly behind the jet nozzle. The pressure profiles in figures 22a–24a support this conclusion, as there is little observed difference in the shape of the pressure profiles along the $\phi = 180^\circ$ and $\phi = 150^\circ$ locations. Differences observed at the other azimuthal locations are primarily due to the passage of the horseshoe vortices, whose location is directly impacted by the prediction of the forward separation and attachment locations. A detailed analysis of the flow structure due to the shock-boundary layer interaction with the jet in a crossflow is given by Dickmann and Lu (28, 29).

4. Summary and Conclusions

Computational fluid dynamic predictions of surface pressure resulting from lateral jet injection into supersonic crossflow from two CCF missile configurations were presented. Predictions were completed for various flow conditions, jet nozzle configurations, missile angles of attack, and jet pressure ratios. Predictions of the longitudinal and azimuthal pressure profiles along the missile body for both the ISL and DLR missile configurations were very good to excellent using the MBL model. No experimental force and moment data were available, but the present CFD results compared favorably with earlier CFD results reported by ISL.

The effects of turbulence model on the jet near- and far-field surface pressures and the resulting aerodynamic force and moment data were presented. Although some turbulence models give significantly different surface pressures, the integrated effects in terms of the aerodynamic forces and moments showed variation of 4%, or less. This is very encouraging from the standpoint of providing aerodynamic characterization input to flight simulation models, but it may still be possible that there could be larger turbulence model effects on the forces and moments depending on the size and shape of downstream appendages (e.g., tail fins) on the munition. An estimate of the trajectory and strength of the counter-rotating vortex pair showed that there was

little effect of turbulence model on the location of the CVP, but over 30% difference in the maximum induced vorticity on the symmetry plane. The latter difference may be large enough to impact the prediction of the resultant forces and moments if there are fins or other control surfaces in the wake of the CVP.

It should also be noted that the best performing turbulence models reported here are for the CFD⁺⁺ solver using a single species ideal gas. Different results may be obtained for other solver/turbulence model combinations. Therefore, some validation studies should be performed for each solver to be used for such jet interaction studies and repeated for multispecies cases.

5. References

1. Margason, R. J. Fifty Years of Jet in Cross Flow Research. AGARD, *72nd Fluid Dynamics Panel Meeting*, (1), 1993.
2. Mahesh, K. The Interaction of Jets with Crossflow. *Annual Review of Fluid Mechanics* **2013**, 45, 379–407.
3. Spaid, F. W.; Cassel, L. A. Aerodynamics Interference Induced by Reaction Controls. *AGARDograph* (173), December 1973.
4. Champigny, P.; Lacau, R. G. Lateral Jet Control for Tactical Missiles. *Special Course on Missile Aerodynamics; AGARD-R-804*, (3), 1994.
5. DeSpirito, J. Factors Affecting Reaction Jet Interaction Effects on Projectiles; AIAA-2011-3031. Presented at the *29th AIAA Applied Aerodynamics Conference*, Honolulu, HI, June 2011.
6. DeSpirito, J. Lateral Jet Interaction on a Finned Projectile in Supersonic Flow; AIAA-2012-0413. Presented at the *50th AIAA Aerospace Sciences Meeting*, Nashville, TN, January 2012.
7. DeSpirito, J. *Lateral Reaction Jet Flow Interaction Effects on a Generic Fin-Stabilized Munition in Supersonic Crossflows*; ARL-TR-6707; U.S. Army Research Laboratory: Aberdeen Proving Ground, MD, November 2013.
8. Hassan, E.; Boles, J.; Aono, H.; Davis, D.; Shyy, W. Supersonic Jet and Crossflow Interaction: Computational Modeling. *Progress in Aerospace Sciences* **2013**, 57, 1–24.
9. Gnemmi, P.; Schafer, H. J. Experimental and Numerical Investigations of a Transverse Jet Interaction on a Missile Body; AIAA-2005-0052. *Presented at the 43rd AIAA Aerospace Sciences Meeting*, Reno, NV, January 2005.
10. Gnemmi, P.; Adeli, R.; Longo, J. Computational Comparisons of the Interaction of a Lateral Jet on a Supersonic Generic Missile; AIAA-2008-6883. Presented at the *AIAA Atmospheric Flight Mechanics Conference*, Honolulu, HI, August 2008.
11. Gnemmi, P.; Eichhorn, A.; Emunds, H.; Esch, H.; Gulhan, A.; Leopold, F.; Schafer, H. J.; Experimental and Computational Study of the Interaction Between a Lateral Jet and the Supersonic External Flow on a Generic Missile Body; PU 622/2006, Institute of Saint-Louis, Saint-Louis, France, May 2006.
12. Stahl, B.; Esch, H.; Gulhan, A. Experimental Investigation of Side Jet Interaction With a Supersonic Cross Flow. *Aerospace Science and Technology* **2008**, 12, 269–275.

13. Adeli, R.; Longo, J. M. A.; Emunds, H. Flow Fields Study of a Supersonic Jet Exiting Into a Supersonic Stream; *Notes on Numerical Fluid Mechanics and Multidisciplinary Design*, Vol. 92, *New Results in Numerical and Experimental Fluid Mechanics V*, Springer, Berlin, GE, 2006, 160–167.
14. Stahl, B.; Emunds, H.; Gulhan, A. Experimental Investigation of Hot and Cold Side Jet Interaction With a Supersonic Cross-Flow. *Aerospace Science and Technology* **2009**, *13*, 488–496.
15. Stahl, B.; Siebe, F.; Gulhan, A. Hot-Gass Side Jet in a Supersonic Freestream. *AIAA Journal of Spacecraft and Rockets* **November/December 2010**, *47*, (6), 957–965.
16. Sourgen, F.; Gauthier, T.; Leopold, F.; Sauerwein, B. Substitution of Hot-Gas Lateral Jets by Cold-Gas Jets in Supersonic Flows. *AIAA Journal of Spacecraft and Rockets*, **January/February 2011**, *48*, (1), 81–92.
17. The Technical Cooperation Program. <http://www.acq.osd.mil/ttcp/> (accessed 27 November 2013).
18. Metacomp Technologies, Inc. MIME User Manual, Agoura Hills, CA, 2008.
19. Metacomp Technologies, Inc. CFD ++ User Manual, Agoura Hills, CA, 2012.
20. Menter, F. R. Two-Equation Eddy-Viscosity Turbulence Models for Engineering Applications. *AIAA Journal* **August 1994**, *32*, (8), 1598–1605.
21. Wilcox, D. C. Formulation of the k-omega Turbulence Model Revisited. *AIAA Journal* **November 2008**, *46*, (11), 2823–2838
22. Spalart, P. R.; Allmaras, S. R. A One-Equation Turbulence Model for Aerodynamic Flows. *Recherche Aerospaciale* **1994**, (1), 5–21.
23. Shur, M. L.; Strelets, M. K.; Travin, A. K.; Spalart, P. R. Turbulence Modeling in Rotating and Curved Channels: Assessing the Spalart-Shur Correction. *AIAA Journal*, **May 2000**, *38*, (5), 784–792
24. Chien, K-Y. Predictions of Channel and Boundary Layer Flows with a Low-Reynolds-Number Turbulence Model. *AIAA Journal* **January 1982**, *20*, (1), 33–38.
25. Goldberg, U.; Batten, P.; Palaniswamy, S.; Chakravarthy, S.; Perroomian, O. Hypersonic Flow Predictions Using Linear and Nonlinear Turbulence Closures. *AIAA Journal of Aircraft* **July/August 2000**, *37*, (4), 671–675.
26. Goldberg U.; Perroomian, O.; Chakravarthy, S. Application Of The $k-\varepsilon-R$ Turbulence Model To Wall-Bounded Compressive Flows; AIAA 98-0323. Presented at the *36th AIAA Aerospace Sciences Meeting*, January 1998.

27. U.S. Army Research Laboratory DOD Supercomputing Resource Center.
<http://www.arl.hpc.mil/index.html/> (accessed 27 November 2013).
28. Dickmann, D. A.; Lu, F. K. Shock/Boundary Layer Interaction Effects of Transverse Jets in Crossflow Over a Body of Revolution; AIAA-2009-4146; Presented at the *19th AIAA Computational Fluid Dynamics Conference*, San Antonio, TX, June 2009.
29. Dickmann, D. A.; Lu, F. K. Shock/Boundary Layer Interaction Effects of Transverse Jets in Crossflow over a Flat Plate. *AIAA Journal of Spacecraft and Rockets* **November/December 2009**, 46, (6), 1132–1141.

List of Symbols, Abbreviations, and Acronyms

3-D	three-dimensional
ARL	U.S. Army Research Laboratory
C_{A0}	axial force coefficient
CCF	cone-cylinder-flare
CFD	computational fluid dynamics
C_p	pressure coefficient
$C_{p\text{no-jet}}$	pressure coefficient for case with no jet injection
$C_{m(0)}$	pitching moment about nose of missile
C_N	normal force coefficient
CVP	counter-rotating vortex pair
cke	cubic k - ε turbulence model
D	diameter of cylindrical section of missile, m
DLR	German Aerospace Center
d	jet nozzle diameter, m
F_{A0}	axial force, N
F_j	jet thrust force, N
F_{ji}	jet interaction force, N
$F_{\text{no-jet}}$	normal force due to α without jet, N
F_{total}	total normal force (thrust + interaction + force due to α), N
ISL	Institute of Saint-Louis
I_t	turbulent intensity
JI	jet interaction
K_f	jet force amplification factor
K_m	jet moment amplification factor

k	turbulent kinetic energy, $\text{m}^2\text{-s}^{-2}$
keR	Goldberg's k - ε - R turbulence model
kw	standard k - ω turbulence model
l_j	distance between missile center of gravity and jet nozzle axis, m
l_t	turbulent length scale, m
M	Mach number
MBL	Menter's baseline turbulence model
M_j	moment induced by jet thrust force, N-m
M_{ji}	moment about MRP induced by jet interaction force, N-m
$M_{ji(0)}$	moment about missile nose induced by jet interaction force, N-m
MRP	moment reference point
M_{total}	moment induced by total normal force, N-m
NJ	no-jet; simulation without jet injection
PIV	particle image velocimetry
PR	jet total-to-freestream static pressure ratio, p_{0j} / p_{∞}
p_{∞}	freestream static pressure, Pa
p_0	freestream total pressure, Pa
p_{0j}	jet total pressure, Pa
Re	Reynolds number
R_t	undamped eddy viscosity
rke	realizable k - ε turbulence model
rkw	realizable k - ω turbulence model
SA	Spalart-Allmaras turbulence model
SARC	Spalart-Allmaras turbulence model with rotation and curvature corrections
SST	Menter's Shear Stress Transport turbulence model
STD	Standard deviation
T_{∞}	freestream static temperature, K

T_0	freestream total temperature, K
TM	turbulence model
X	axial distance along missile, m
X_{cp}	center of pressure location relative to missile nose, calibers
y^+	nondimensional wall distance
α	angle of attack, °
ε	eddy diffusivity, m ² -s ⁻¹
ϕ	azimuthal distance around missile body, °
ρ_∞	freestream gas density, kg-m ⁻³
ω	specific dissipation, s ⁻¹

1 DEFENSE TECHNICAL
(PDF) INFORMATION CTR
DTIC OCA

2 DIRECTOR
(PDF) US ARMY RSRCH LAB
RDRL CIO LL
IMAL HRA MAIL & RECORDS MGMT

1 GOVT PRINTG OFC
(PDF) A MALHOTRA

6 RDECOM AMRDEC
(PDF) L AUMAN
J DOYLE
S N DUNBAR
B E GRANTHAM
M MCDANIEL
C ROSEMA

16 RDECOM ARDEC
(PDF) D CARLUCCI
S CHUNG
D CLER
M DUCA
L FLORIO
J GRAU
M HOLLIS
W KOENIG
A LICHTENBERG-SCANLAN
G MALEJKO
T RECCHIA
C STOUT
W TOLEDO
J TRAVAILLE
E VAZQUEZ
C WILSON

4 PM CAS
(PDF) M BURKE
R KIEBLER
P MANZ
G SCHWARTZ

3 PM MAS
(PDF) J FOULTZ
C GRASSANO
D RIGOGLIOSO

1 AEROPREDICTION INC
(PDF) F MOORE

1 ARROW TECH
(PDF) W HATHAWAY

4 ATK
(PDF) B BASEGHI
R DOHRN
S OWENS
A SAIDI

1 GEORGIA INSTITUTE
(PDF) OF TEHCNOLOGY
M COSTELLO

1 VILLANOVA UNIVERSITY
(PDF) K FOULADI

1 NASA LANGLEY RSRCH CTR
(PDF) S VIKEN

3 NAVAIR
(PDF) D FINDLAY
J LEE
T SHAFER

2 NAWCWD
(PDF) P CROSS
R SCHULTZ

1 AFOSR EOARD
(PDF) G ABATE

2 NSWC DAHLGREN
(PDF) L STEELMAN
K PAMADI

2 DEFENCE RSRCH AND DEV
(PDF) CANADA (DRDC)
D CORRIVEAU
N HAMEL

3 DEFENCE SCI AND TECHLGY LAB
(PDF) (DSTL)
R CHAPLIN
B SHOESMITH
T BIRCH

3 DEFENCE SCI AND TECHLGY
(PDF) ORGANIZATION (DSTO)
S HENBEST
M GIACOBELLO
B WOODYATT

1 DEFENCE TECHLGY AGENCY (DTA)
(PDF) N WILLIAMS

2 INSTITUTE SAINT LOUIS (ISL)
(PDF) C BERNER
P GNEMMI

ABERDEEN PROVING GROUND

40 DIR USARL
(PDF) RDRL CI
P PLOSTINS
RDRL WM
P BAKER
R EHLERS
RDRL WML
P PEREGINO
M ZOLTOSKI
RDRL WML A
W OBERLE
L STROHM
RDRL WML B
N TRIVEDI
RDRL WML C
S AUBERT
RDRL WML D
R BEYER
M NUSCA
RDRL WML E
V BHAGWANDIN
I CELMINS
J DESPIRITO
L FAIRFAX
F FRESCONI
J GARNER
B GUIDOS
K HEAVEY
R KEPPINGER
G OBERLIN
T PUCKETT
J SAHU
S SILTON
P WEINACHT
RDRL WML F
G BROWN
J CONDON
B DAVIS
B KLINE
J MALEY
B NELSON
B TOPPER
RDRL WML G
M CHEN
C EICHHORST
M MINNICINO
J SOUTH
RDRLWML H
J NEWILL

RDRL WMM
J ZABINSKI
RDRL WMP
D LYON
RDRL WMP G
R BANTON

INTENTIONALLY LEFT BLANK.